Article

Developmental Cell

Ubiquitin-dependent remodeling of the actin cytoskeleton drives cell fusion

Graphical Abstract

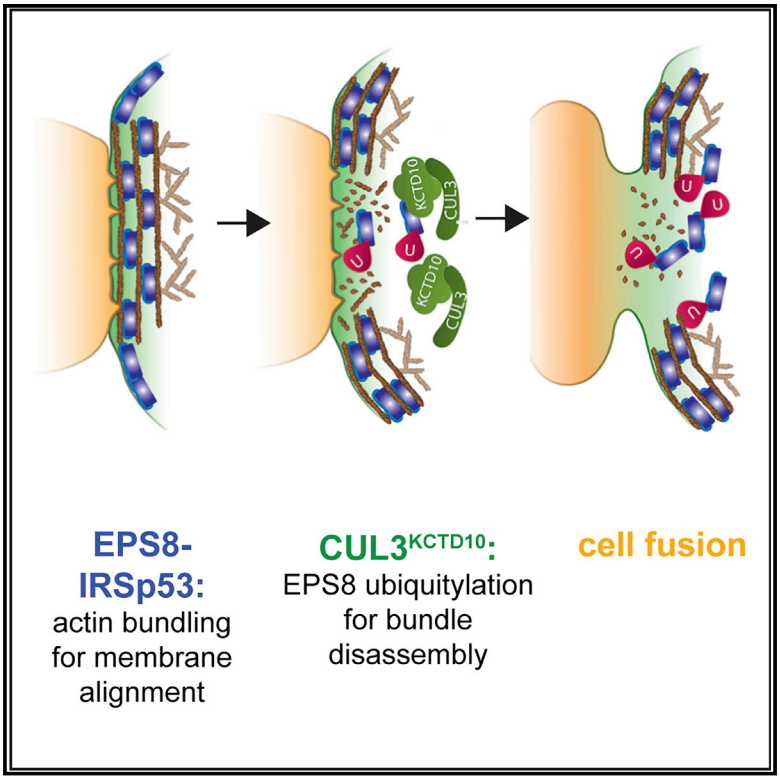

Authors

Fernando Rodríguez-Pérez, Andrew G. Manford, Angela Pogson, Andrew J. Ingersoll, Brenda Martínez-González, Michael Rape

Correspondence

mrape@berkeley.edu

In Brief

Rodríguez-Pérez et al. report a ubiquitin-dependent toggle switch, built around the E3 ligase $CUL3^{KCTD10}$ and its substrate, EPS8-IRSp53, which controls actin bundling at sites of cell contact as an essential step in myogenic cell fusion.

Highlights

- The conserved E3 ligase $CUL3^{KCTD10}$ is essential for myoblast fusion
- $CUL3^{KCTD10}$ ubiquitylates EPS8 to displace the actin bundler from cell contact sites
- $CUL3^{KCTD10}$ also inhibits the activity of EPS8-IRSp53 in actin bundling
- This ubiquitin-dependent toggle switch pushes fusion beyond membrane apposition

Rodríguez-Pérez et al., 2021, Developmental Cell *56*, 1–14
March 8, 2021
https://doi.org/10.1016/j.devcel.2021.01.016

CellPress

Please cite this article in press as: Rodríguez-Pérez et al., Ubiquitin-dependent remodeling of the actin cytoskeleton drives cell fusion, Developmental Cell (2021), https://doi.org/10.1016/j.devcel.2021.01.016

Developmental Cell

CellPress

Article

Ubiquitin-dependent remodeling of the actin cytoskeleton drives cell fusion

Fernando Rodríguez-Pérez,[1,2] Andrew G. Manford,[2] Angela Pogson,[2] Andrew J. Ingersoll,[2] Brenda Martínez-González,[2] and Michael Rape[1,2,3,*]

[1]Howard Hughes Medical Institute, University of California at Berkeley, Berkeley, CA 94720, USA
[2]Department of Molecular and Cell Biology, University of California at Berkeley, Berkeley, CA 94720, USA
[3]Lead contact
*Correspondence: mrape@berkeley.edu
https://doi.org/10.1016/j.devcel.2021.01.016

SUMMARY

Cell-cell fusion is a frequent and essential event during development, and its dysregulation causes diseases ranging from infertility to muscle weakness. Fusing cells need to repeatedly remodel their plasma membrane through orchestrated formation and disassembly of actin filaments, but how the dynamic reorganization of the cortical actin cytoskeleton is controlled is still poorly understood. Here, we identified a ubiquitin-dependent toggle switch that establishes reversible actin bundling during mammalian cell fusion. We found that EPS8-IRSp53 complexes stabilize cortical actin bundles at sites of cell contact to promote close membrane alignment. EPS8 monoubiquitylation by $CUL3^{KCTD10}$ displaces EPS8-IRSp53 from membranes and counteracts actin bundling, a dual activity that restricts actin bundling to allow paired cells to progress with fusion. We conclude that cytoskeletal rearrangements during development are precisely controlled by ubiquitylation, raising the possibility of modulating the efficiency of cell-cell fusion for therapeutic benefit.

INTRODUCTION

Approximately one-third of the cells in our bodies have fused with other cells and contain multiple nuclei (Brukman et al., 2019). Cell-cell fusion (henceforth referred to as cell fusion) occurs at the beginning of life during fertilization and continues to be required for placenta formation, generation of bone-resorbing osteoclasts, and the development of myofibers or giant cells of the macrophage lineage (Petrany and Millay, 2019). As a consequence of its role during tissue formation, loss of cell fusion is incompatible with life, and mutations that render this process inefficient cause infertility (Yu et al., 2018), muscle weakness (Di Gioia et al., 2017), or osteopetrosis (Pereira et al., 2018).

Many insights into mechanisms of cell fusion were gained from studies of multinucleated myotubes, the most prevalent tissue in mammals (Deng et al., 2017; Lee and Chen, 2019; Lehka and Rędowicz, 2020). Both myotube growth and repair rely on their fusion with myoblasts derived from satellite precursors under the basal lamina of muscle fibers. Fusion-competent myoblasts migrate toward a myotube to establish adhesion, which initially keeps the plasma membranes of cells ~50 nm apart (Dhanyasi et al., 2015; Galletta et al., 2004; Özkan et al., 2014; Rosen et al., 1992; Ruiz-Gómez et al., 2000; Segal et al., 2016). The myoblast then aligns with the myotube to form a fusogenic synapse and achieve closer contact that is referred to as membrane apposition (Kim and Chen, 2019; Lee and Chen, 2019). Myoblasts subsequently project multiple protrusions toward the myotube, which in turn provides mechanical resistance necessary for fusion (Kim et al., 2015; Lee and Chen, 2019). The juxtaposition of apposed cells enables fusogens, such as Myomaker and Myomixer, to form a fusion pore that initiates membrane and cytoplasmic mixing (Bi et al., 2017; Millay et al., 2013; Quinn et al., 2017; Zhang et al., 2017).

To successfully execute the fusion program, cells frequently need to reshape their plasma membrane by remodeling their actin cytoskeleton (Deng et al., 2017). Accordingly, multiple actin structures fulfill critical roles during cell fusion (Lee and Chen, 2019). Branched actin networks in myoblasts generate a large actin focus, which sprouts actin-filled protrusions toward the myotube (Sens et al., 2010). These protrusions are met by a cortical actomyosin sheet in myotubes, which provides necessary mechanical resistance (Kim et al., 2015). Conversely, actin bundles are constituents of filopodia used by myotubes of the developing *Drosophila* adult muscle to capture myoblasts and accomplish cell adhesion (Dhanyasi et al., 2015; Segal et al., 2016). In line with these observations, genetic screens in flies have identified regulators of actin filament nucleation, branching, or bundling, including the Scar/WAVE complex, the WASP complex, or Dynamin, as components of the fusion machinery (Dhanyasi et al., 2015; Kim et al., 2007; Massarwa et al., 2007; Richardson et al., 2007; Schäfer et al., 2007; Segal et al., 2016; Zhang et al., 2020). Whether similar players shape the actin cytoskeleton during mammalian cell fusion is less well understood.

While assembly of actin filaments has long been studied, the cytoskeletal rearrangements during cell fusion also require the timely dismantling of actin structures that have fulfilled their

Please cite this article in press as: Rodríguez-Pérez et al., Ubiquitin-dependent remodeling of the actin cytoskeleton drives cell fusion, Developmental Cell (2021), https://doi.org/10.1016/j.devcel.2021.01.016

functions. For example, the actin focus in myoblasts persists for only ~11 min (Deng et al., 2017; Richardson et al., 2007). If disassembly of filaments or bundles is prevented, the fusion program cannot proceed through its multiple steps and the merger of cells is aborted (Deng et al., 2016, 2015; Geisbrecht et al., 2008; Haralalka et al., 2014). While actin polymerization can be tuned down (Doherty et al., 2011), it is still unclear whether existing actin structures are actively dismantled in a regulated manner. How the actin cytoskeleton adapts to the dynamic needs of cell fusion therefore remains to be elucidated.

Here, we have identified the conserved E3 ligase CUL3^{KCTD10} and its monoubiquitylation target, EPS8, as key regulators of reversible actin bundling and cell fusion. When bound to IRSp53 (also known as BAIAP2), EPS8 promotes the formation of cortical actin bundles required for membrane apposition and fusion. Conversely, CUL3^{KCTD10} displaces EPS8-IRSp53 from sites of cell contact, shuts down its bundling activity, and helps dismantle existing actin bundles. Its dual activity in controlling EPS8-IRSp53 localization and function allows CUL3^{KCTD10} to establish a ubiquitin-dependent toggle switch that restricts actin bundling and thereby guides cell fusion beyond membrane apposition. We conclude that ubiquitylation regulates cytoskeletal rearrangements during development, which may provide opportunities for counteracting aberrant actin bundling or cell fusion during disease.

RESULTS

KCTD10 is required for myoblast fusion

C2C12 cells, which can undergo rapid differentiation from a myoblast stage with single nuclei into multinucleate myotubes, provide a powerful system to discover regulators of cell fusion. In line with previous work (Bi et al., 2017), we noted that inhibition of C2C12 fusion upon depletion of Myomixer caused formation of cells that were mononucleate yet expressed the late differentiation marker, myosin heavy chain (MyHC) (Figure S1A). This phenotype could be quantified as an increased average ratio between the short and long axes of MyHC-positive cells (R_{MyHC}), which provided a robust readout for genetic screens that dissect cell fusion (Figure S1B).

Having established this screening platform, we depleted ~150 substrate adaptors of CUL2 and CUL3 E3 ligases from myoblasts and searched for the increase in R_{MyHC} that is indicative of defective cell fusion. We focused on E3 ligases, as they control metazoan development and are mutated in distal and nemaline myopathies (Gupta and Beggs, 2014; Rape, 2018). Moreover, tissue-specific deletion of *CUL3* prevented myoblast fusion in mice (Blondelle et al., 2019; Papizan et al., 2018). Our screen identified a single CUL3 adaptor, KCTD10, whose loss dramatically inhibited myoblast fusion (Figure 1A). We confirmed with individual small interfering RNAs (siRNAs) that KCTD10 depletion sharply increased the number of mononucleate MyHC-positive cells (Figure 1B), similar to loss of Myomixer (Figures S1A and S1B). Highlighting the specificity of these results, the close KCTD10 homologs KCTD13 and TNFAIP1 were not required for cell fusion (Figure S1C). Fusion of KCTD10-depleted cells was restored by the expression of siRNA-resistant KCTD10, even if it had been induced days after differentiation had begun and MyHC had already been expressed (Figures 1B and 1C). A KCTD10 variant, KCTD10$^{\Delta CUL3}$, that was unable to bind CUL3, did not support myotube formation, showing that ubiquitylation is required for cell fusion (Figures 1B, 1C, and S1D).

Myogenic cell fusion is an asymmetric process between attacking myoblasts and receiving myotubes (Lee and Chen, 2019). To determine which population required CUL3^{KCTD10}, we labeled myoblasts or myotubes with distinct dyes, independently depleted KCTD10, and monitored fusion of mixed cells by fluorescence microscopy. If both myoblasts and myotubes were treated with control siRNAs, fusion occurred efficiently, and multinucleated cells labeled by both dyes were readily detected (Figure 1D). While similar observations were made upon depletion of KCTD10 from myoblasts, its loss from myotubes strongly impaired cell fusion (Figure 1D). Thus, KCTD10 is required within the receiving myotube to promote cell fusion.

Despite its striking effects on cell fusion, depletion of KCTD10 did not strongly impact the gene expression program of myotube specification (Figure 1E). Protein levels of differentiation markers, such as Myogenin, MyHC, or Myomixer, were also unaffected by the loss of this CUL3 adaptor (Figures S1E and S1F), and KCTD10 was not required for myoblast division or survival (Figure S1G). We, therefore, conclude that CUL3^{KCTD10}, whose specificity component KCTD10 is highly conserved from flies to humans (Figure S1H), is an important regulator of myogenic cell fusion.

CUL3^{KCTD10} targets the EPS8-IRSp53 complex

We developed an integrated approach to identify proteins that CUL3^{KCTD10} must ubiquitylate for cell fusion to occur. First, we appended a 3xFLAG epitope to the myoblast *KCTD10* locus (Figure S2A). This allowed us to purify endogenous KCTD10^{3xFLAG} from cells treated with MLN4924, an inhibitor of neddylation that prevents substrate turnover by Cullin-RING ligases (CRLs) and should trap targets on KCTD10 (Bennett et al., 2010). We also isolated interactors of KCTD10$^{\Delta CUL3}$, which can bind, but not ubiquitylate, its substrates, a feature that had improved association of other CRLs with their targets (Manford et al., 2020; Mena et al., 2018; Werner et al., 2018, 2015). Finally, we searched for interactors of KCTD10^{UBA}, in which ubiquitin-binding UBA-domains provided KCTD10 with an additional recognition site for ubiquitylated substrates (Mark et al., 2016; Oh et al., 2020). We expected that substrates of CUL3^{KCTD10} were enriched in purifications of endogenous KCTD10 in the presence of MLN4924, by KCTD10$^{\Delta CUL3}$ compared with wild-type KCTD10, as well as by KCTD10^{UBA}.

These experiments converged on a small set of candidate CUL3^{KCTD10} substrates that was dominated by regulators of the actin cytoskeleton (Figure 2A). These included members of the α-actinin family of actin bundlers (ACTN1, ACTN3, and ACTN4) (Ribeiro et al., 2014), whose aberrant regulation interferes with myoblast fusion (Blondelle et al., 2019). We also detected two proteins, EPS8 and IRSp53, which preferentially bound KCTD10 in the presence of MLN4924 and were enriched in purifications of KCTD10$^{\Delta CUL3}$ and KCTD10^{UBA}. The conserved EPS8 and IRSp53 interact with each other to form a complex that, similar to α-actinin, promotes actin-bundling (Disanza et al., 2006; Funato et al., 2004).

To determine which candidate target mediated the effects of CUL3^{KCTD10} on cell fusion, we considered two potential

Please cite this article in press as: Rodríguez-Pérez et al., Ubiquitin-dependent remodeling of the actin cytoskeleton drives cell fusion, Developmental Cell (2021), https://doi.org/10.1016/j.devcel.2021.01.016

CellPress

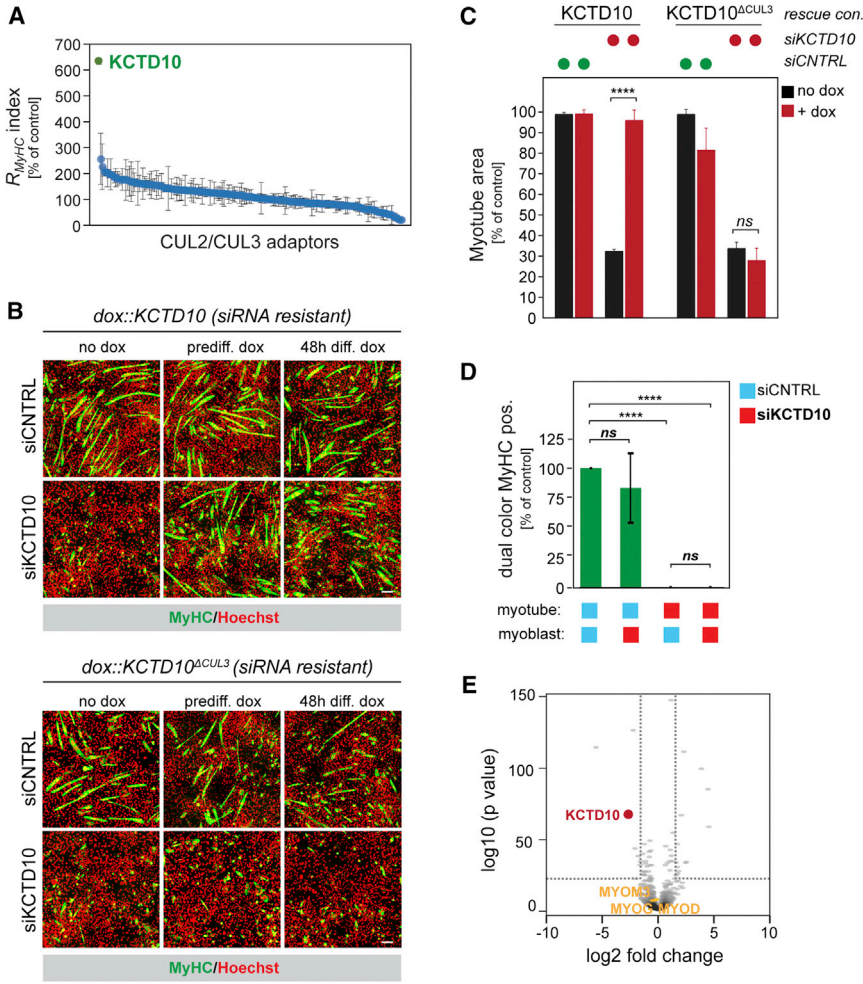

Figure 1. KCTD10 is essential for myoblast fusion

(A) Myoblasts were depleted of substrate adaptors of CUL2 and CUL3 E3 ligases, differentiated, and analyzed for expression of MyHC and cell fusion by automated microscopy.

(B) C2C12 myoblasts were depleted of KCTD10, differentiated, and MyHC expression was analyzed by microscopy. *prediff. dox*: siRNA-resistant wild-type KCTD10 or KCTD10$^{\Delta CUL3}$ were expressed 24 h prior to differentiation. *48h diff. dox*: KCTD10 variants were expressed 48 h after differentiation was initiated.

(C) Quantification of myotube area as a proxy for cell fusion (mean ± SD, three biological replicates; ****$p < 0.0001$, ns = not significant) of KCTD10-depleted myoblasts expressing siRNA-resistant KCTD10 or KCTD10$^{\Delta CUL3}$.

(D) C2C12 myoblasts or differentiated myotubes were independently depleted of KCTD10, treated with fluorescent dyes, and mixed for cell fusion to proceed. MyHC-positive multinucleate cells containing both dyes were quantified (mean ± SD, three biological replicates; ****$p < 0.0001$).

(E) RNA-seq analysis of C2C12 myoblasts that were transfected with either control or KCTD10-siRNA and induced to differentiate. Scale bars are 100 μm.

outcomes of ubiquitylation: if CUL3^{KCTD10} inhibited a key target, loss of this protein should rescue fusion in the absence of KCTD10; by contrast, if ubiquitylation activated a substrate, depletion of this protein itself should phenocopy loss of KCTD10. Consistent with an inhibitory role of ubiquitylation, we found that depletion of EPS8, IRSp53, or the IRSp53 homolog IRTKS (also known as BAIAP2L1), but not α-actinin proteins, rescued fusion of KCTD10-deficient myoblasts (Figures 2B, S2B, and S2C). These results were specific, as siRNA-resistant EPS8 corrected all effects of depleting the endogenous protein (Figure 2C). Loss of the GTPase CDC42, which activates EPS8 and IRSp53 to bundle actin filaments (Kast et al., 2014; Krugmann et al., 2001), also improved fusion of myoblasts lacking KCTD10, while depletion of Mena or SOS, two EPS8-and IRSp53-binding partners that do not bundle filaments along their length, did not have this outcome (Figure S2D). A reduction of EPS8 levels did not rescue fusion of cells lacking Myomixer (Figure S2E).

Depletion of EPS8 or IRSp53 by themselves did not interfere with myoblast differentiation nor did such treatment inhibit fusion of myoblasts into multinucleated myotubes (Figures 2B and 2D). This was mirrored by the α-actinin proteins, which were not required for myoblast fusion. However, consistent with actin bundlers compensating for each other (Mogilner and Rubinstein, 2005), co-depletion of EPS8 and α-actinin strongly inhibited myoblast fusion (Figures 2D and S2F). Thus, actin bundling by either EPS8-IRSp53 or α-actinin promotes myoblast fusion, yet CUL3^{KCTD10} is specifically required to restrict EPS8-IRSp53 activity during this process.

CUL3^{KCTD10} monoubiquitylates EPS8

Affinity-purification experiments confirmed that endogenous EPS8 robustly bound IRSp53 and KCTD10 (Figure 3A). To reconstitute substrate binding by KCTD10 *in vitro*, we purified KCTD10, which forms a tetramer (Pinkas et al., 2017), from bacteria or C2C12 cells and incubated it with candidate targets produced by *in vitro* transcription and translation. We found that EPS8, IRSp53, and IRTKS, but not control proteins, were efficiently retained by KCTD10 (Figures 3B and S3A). In addition, we mixed purified KCTD10, EPS8, and IRSp53 and observed by size exclusion chromatography that they formed a complex containing all proteins (Figure 3C). Truncation analyses showed that EPS8 bound KCTD10 through either half of its lipid-binding split-pleckstrin homology (PH), while IRSp53 employed its amino-terminal BAR-like IMD domain for the same purpose (Figures 3D–3F). KCTD10 therefore directly engages the EPS8-IRSp53 complex

Please cite this article in press as: Rodríguez-Pérez et al., Ubiquitin-dependent remodeling of the actin cytoskeleton drives cell fusion, Developmental Cell (2021), https://doi.org/10.1016/j.devcel.2021.01.016

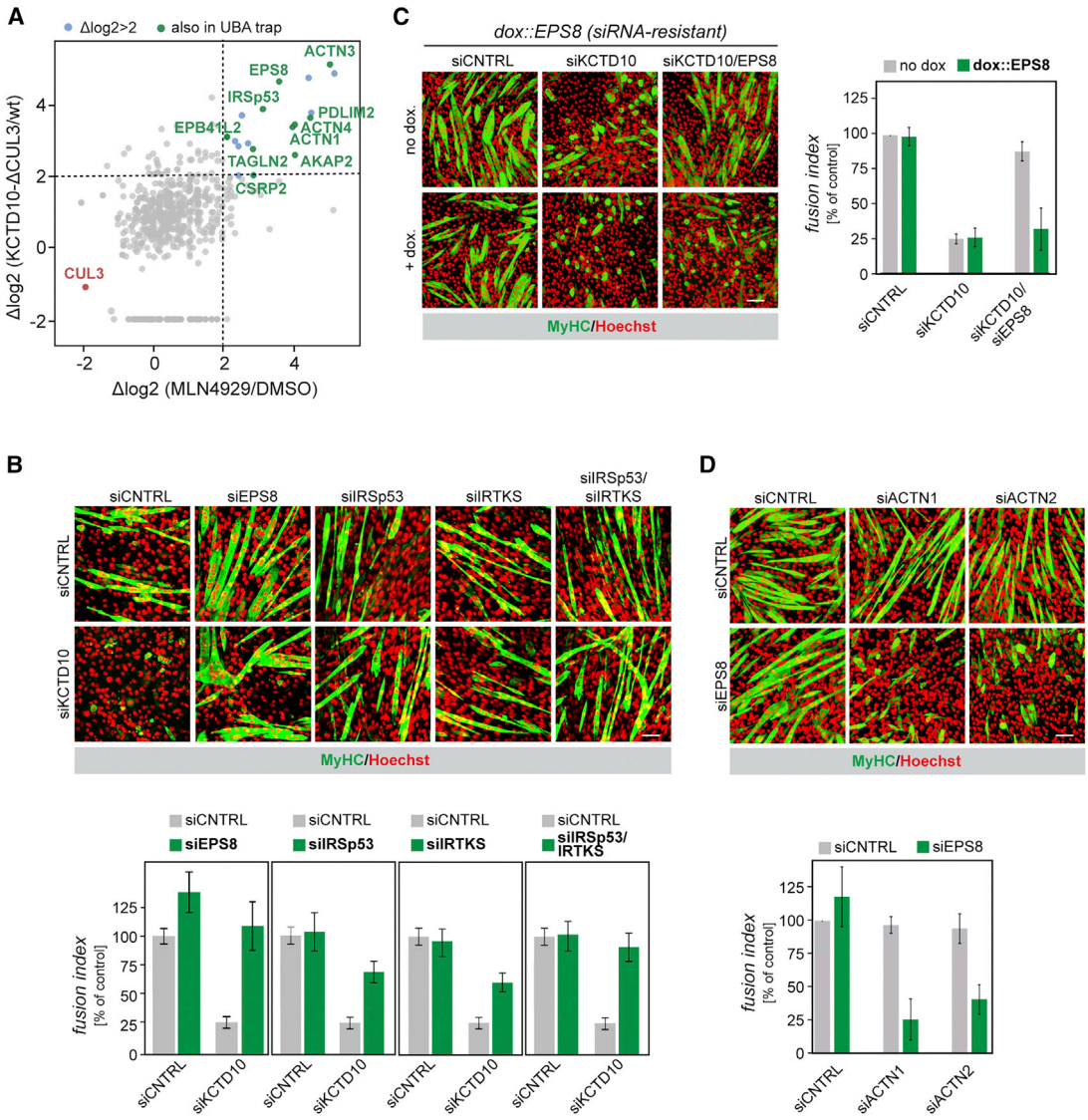

Figure 2. CUL3^{KCTD10} targets EPS8-IRSp53 during cell fusion

(A) Proteomic identification of CUL3^{KCTD10} substrates, comparing normalized total spectral counts (TSCs) of endogenous KCTD10^{FLAG} purifications ± MLN4924 with purifications of KCTD10 and KCTD10$^{\Delta CUL3}$. Proteins detected in KCTD10^{UBA} purifications are marked green. Actin regulators are labeled.

(B) Candidate CUL3^{KCTD10} targets were depleted from control cells or cells lacking KCTD10, and myoblast fusion was followed by microscopy of MyHC and Hoechst. Errors bars represent the mean ± SD.

(C) Cell fusion was analyzed upon differentiation of myoblasts lacking KCTD10 or KCTD10 and EPS8. siRNA-resistant EPS8 was expressed as indicated. Errors bars represent the mean ± SD.

(D) C2C12 myoblasts were depleted of EPS8 and ACTN1/2 as indicated, differentiated, and analyzed by microscopy against MyHC and Hoechst. Scale bars are 100 μm. Errors bars represent the mean ± SD.

through substrate domains that are typically involved in membrane recruitment.

Importantly, recombinant NEDD8-modified CUL3^{KCTD10} efficiently decorated EPS8 with one or two ubiquitin molecules (Figure 3G). Despite being present in the same reaction, IRSp53 was not ubiquitylated. Experiments with methylated ubiquitin, which cannot form ubiquitin polymers, confirmed that CUL3^{KCTD10} primarily monoubiquitylated EPS8 (Figure 3H), with one site being within the substrate's split-PH domain (Figure S3B). CUL3^{KCTD10} also monoubiquitylated α-actinin (Figure S3C), which together showed that CUL3^{KCTD10} binds and monoubiquitylates two actin bundlers, EPS8 and α-actinin. As only EPS8 modification was critical for cell fusion, we focused subsequent analyses on the role of the EPS8-IRSp53 complex, as well as of EPS8 ubiquitylation, during this process.

CUL3^{KCTD10} restricts membrane localization of EPS8

As expected for monoubiquitylation (Oh et al., 2018), KCTD10 depletion did not affect EPS8 or IRSp53 stability (Figure S4A). We therefore asked whether CUL3^{KCTD10} instead controls

Please cite this article in press as: Rodríguez-Pérez et al., Ubiquitin-dependent remodeling of the actin cytoskeleton drives cell fusion, Developmental Cell (2021), https://doi.org/10.1016/j.devcel.2021.01.016

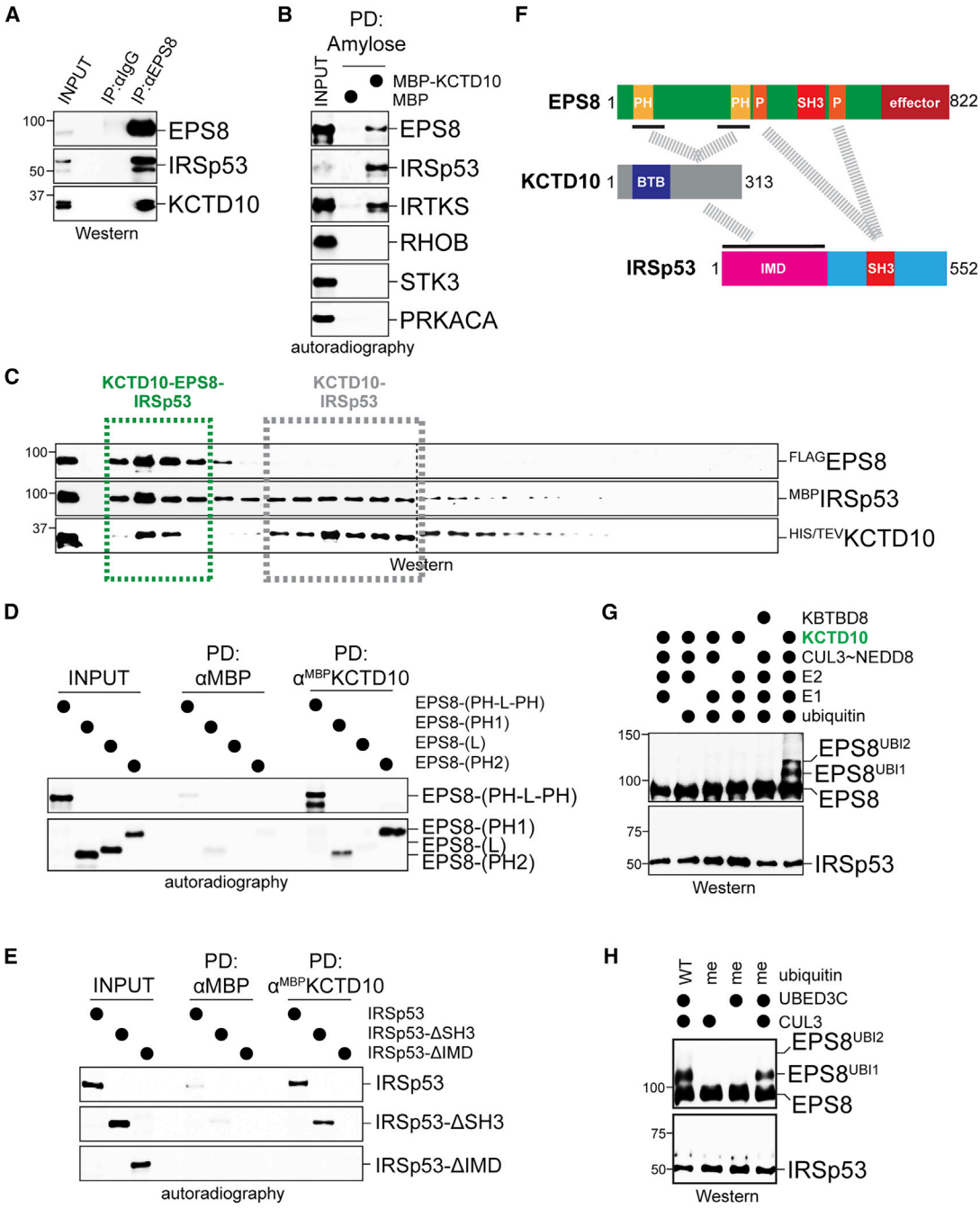

Figure 3. CUL3^{KCTD10} monoubiquitylates EPS8

(A) Endogenous EPS8 was affinity-purified from C2C12 cells and tested for co-precipitating IRSp53 and KCTD10 by western blotting.

(B) Immobilized ^{MBP}KCTD10 purified from bacteria was incubated with ^{35}S-labeled EPS8, IRSp53, or IRTKS produced by *in vitro* transcription/translation, and bound proteins were detected by gel electrophoresis and autoradiography.

(C) Recombinant KCTD10, EPS8, and IRSp53 were mixed and analyzed for ternary-complex formation (green) by size exclusion chromatography. A binary KCTD10-IRSp53 was also detected (gray).

(D) ^{35}S-labeled EPS8 truncations were incubated with immobilized ^{MBP}KCTD10 and bound proteins were detected as described above.

(E) ^{35}S-labeled IRSp53 truncations were incubated with immobilized ^{MBP}KCTD10 and bound proteins were detected as described above.

(F) Summary of domain interactions between KCTD10, EPS8, and IRSp53.

(G) Ubiquitylation of recombinant EPS8-IRSp53 was monitored by western blotting after incubation with NEDD8-modified CUL3^{KCTD10}, E1, E2, and ubiquitin.

(H) EPS8-IRSp53 was incubated with NEDD8-modified CUL3^{KCTD10} and wild-type or methylated ubiquitin, as indicated.

Please cite this article in press as: Rodríguez-Pérez et al., Ubiquitin-dependent remodeling of the actin cytoskeleton drives cell fusion, Developmental Cell (2021), https://doi.org/10.1016/j.devcel.2021.01.016

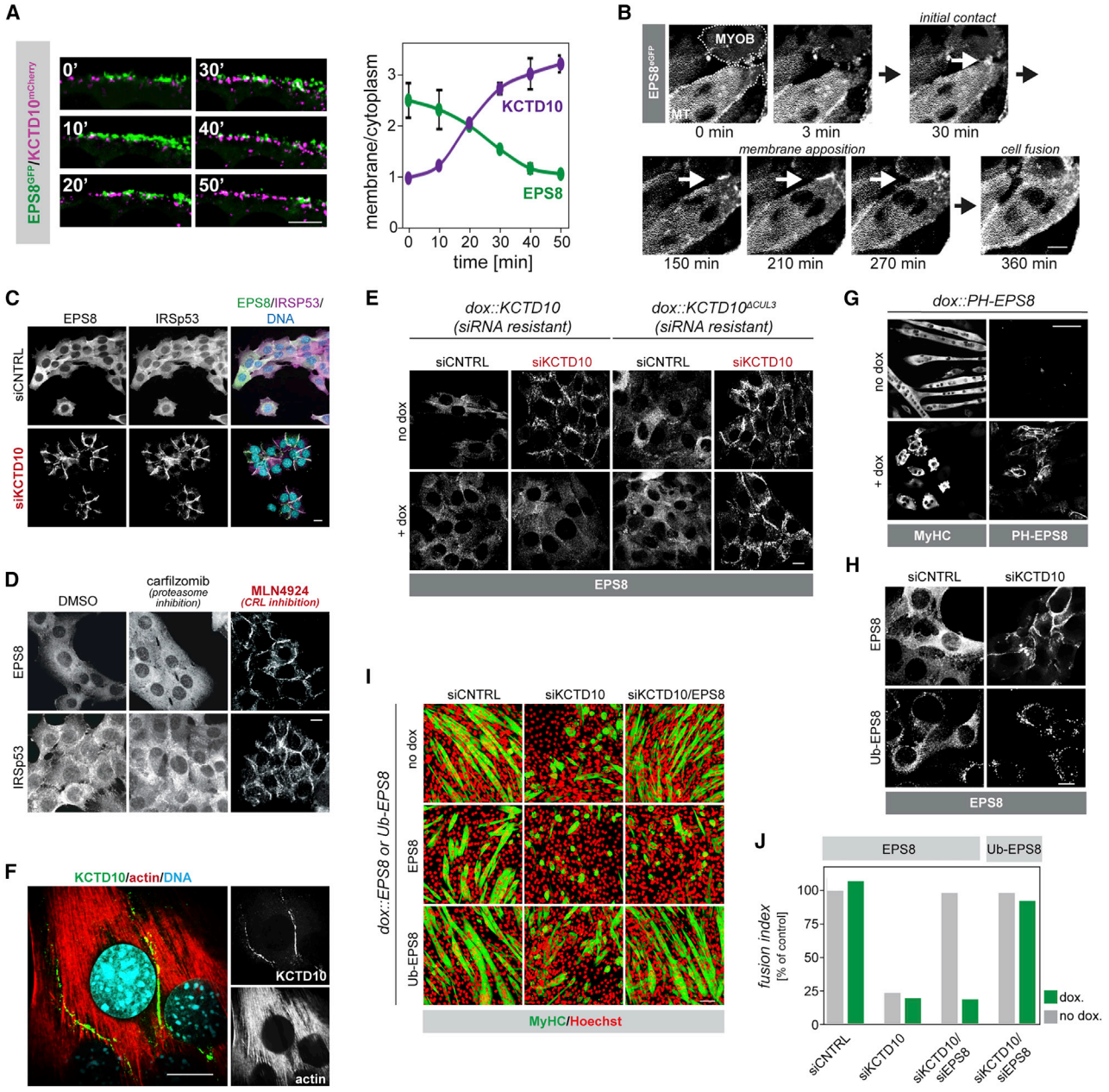

Figure 4. CUL3^{KCTD10} displaces EPS8-IRSp53 from cell contact sites

(A) Live cell imaging of plasma membranes of C2C12 myoblasts stably expressing EPS8^{eGFP} and KCTD10^{mCherry}. Right: quantification of membrane accumulation of EPS8 (green) and KCTD10 (purple), normalized to maximum EPS8 membrane binding (n = 3, Errors bars represent the mean ± SD).

(B) Localization of stable expressed EPS8^{eGFP} was monitored in differentiating C2C12 myoblasts by live cell imaging.

(C) Localization of endogenous EPS8 and IRSp53 was analyzed by immunofluorescence microscopy in C2C12 myoblasts depleted of KCTD10 as indicated.

(D) C2C12 myoblasts were treated with proteasome inhibitor, carfilzomib, or CRL inhibitor, MLN4924, and analyzed for localization of endogenous EPS8 and IRSp53 by immunofluorescence microscopy.

(E) Expression of wild-type KCTD10, but not catalytically inactive KCTD10^{ΔCUL3}, in cells depleted of endogenous KCTD10 reverts accumulation of EPS8 at cell contact sites.

(F) Endogenous KCTD10 accumulates in myoblasts at cell contact sites, as determined by microscopy.

(G) EPS8 was targeted to plasma membranes of C2C12 myoblasts by fusion to a tandem PH domain of PLCδ and cell fusion was monitored by immunofluorescence microscopy against MyHC and EPS8.

(H) Localization of an EPS8-ubiquitin fusion in C2C12 myoblasts treated with control siRNAs or siRNAs targeting KCTD10. Exogenously expressed EPS8 or Ub-EPS8 was detected through an HA-tag.

Please cite this article in press as: Rodríguez-Pérez et al., Ubiquitin-dependent remodeling of the actin cytoskeleton drives cell fusion, Developmental Cell (2021), https://doi.org/10.1016/j.devcel.2021.01.016

EPS8 localization and generated C2C12 myoblasts that stably expressed both EPS8^{eGFP} and KCTD10^{mCherry}. While most EPS8^{eGFP} was detected in the cytoplasm, live cell imaging showed that it could spontaneously translocate to plasma membranes (Figure 4A). Shortly after membrane delivery of EPS8, KCTD10^{mCherry} was recruited to the same site, which was followed by EPS8 displacement (Figure 4A). Trafficking of KCTD10^{mCherry} was disrupted by latrunculin A (Figure S4B), implying that actin filaments, which are stabilized by EPS8-IRSp53 (Disanza et al., 2006), control KCTD10 localization. Live cell imaging of C2C12 cells that only expressed EPS8^{eGFP} and in contrast to doubly tagged cells could be differentiated, showed that EPS8^{eGFP} rapidly translocated to the plasma membrane once contact between fusing cells had been established (Figure 4B). EPS8 was retained at sites of cell contact, as the area shared between cells slowly grew. At the time of cell fusion, EPS8 became diffuse in the now shared cytoplasm.

These observations raised the possibility that transient EPS8 accumulation at the plasma membrane could be regulated by CUL3^{KCTD10}. To test this hypothesis, we depleted KCTD10 and followed endogenous proteins by immunofluorescence microscopy. As with live cell imaging, most EPS8 and IRSp53 were found in the myoblast cytoplasm (Figure 4C). This dramatically changed in the absence of KCTD10, where EPS8 and IRSp53 strongly accumulated at sites of cell contact (Figure 4C). Acute CRL inactivation by MLN4924 also led to an enrichment of EPS8 and IRSp53 at sites of cell contact, while proteasome inhibition had no effect (Figure 4D). Underscoring the specificity of these results, expression of siRNA-resistant KCTD10 but not inactive KCTD10$^{\Delta CUL3}$ prevented the aberrant localization of EPS8 in the absence of endogenous KCTD10 (Figure 4E). We conclude that ubiquitylation by CUL3^{KCTD10} restricts the localization but not the stability of EPS8-IRSp53 at sites of cell contact. In line with this notion, KCTD10 localized in myoblasts or myotubes to cellular interfaces (Figures 4F and S4C).

Our findings suggested that transient recruitment of EPS8 to sites of cell contact promotes cell fusion, while its persistent membrane accumulation interferes with the same process. Indeed, constitutive localization of EPS8 to plasma membranes strongly inhibited myoblast fusion (Figure 4G). If we however mimicked persistent monoubiquitylation by fusing ubiquitin to EPS8, EPS8 was constitutively displaced from sites of cell contact even in KCTD10-depleted cells (Figure 4H). In contrast to wild-type EPS8, introduction of Ub-EPS8 did not prevent the fusion of myoblasts devoid of endogenous KCTD10 and EPS8, showing that ubiquitylated EPS8 is inactive (Figures 4I, 4J, and S4D). We conclude that cell fusion requires the orchestrated recruitment and displacement of EPS8-IRSp53 from sites of cell contact, regulated by CUL3^{KCTD10}.

KCTD10 inhibits actin bundling by EPS8-IRSp53

While re-localization of EPS8-IRSp53 should turn off actin bundling at sites of cell contact, it might lead to deleterious stabilization of actin filaments at other locations. This led us to speculate that release of EPS8-IRSp53 from cellular interfaces should be coupled to inhibition of its activity in actin bundling. To test this hypothesis, we added recombinant EPS8-IRSp53 to pyrene-labeled actin for analysis by microscopy. While EPS8-IRSp53 had little effect on actin polymerization (Figure S5A), it drove formation of parallel actin bundles *in vitro* (Figures 5A and S5B). These bundles differed in appearance from those produced by α-actinin, which stimulated assembly of thicker, yet less parallel, cables (Figure 5A). Strikingly, if we treated EPS8-IRSp53 with CUL3^{KCTD10} to induce EPS8 monoubiquitylation, actin bundling was prevented (Figure 5B).

Our prior analyses had shown that KCTD10, EPS8, and IRSp53 form a stable ternary complex, reminiscent of persistent interactions between other CUL3 ligases and their substrates (McGourty et al., 2016; Tong et al., 2006; Werner et al., 2018, 2015). We therefore also dissected the behavior of recombinant KCTD10-EPS8-IRSp53 toward actin. We noted that the ternary complex containing KCTD10 reduced the amount of actin polymer in a concentration-dependent manner, even if no ubiquitylation could occur (Figures 5C and S5A). As the ternary complex predominantly impacted the maximum extent of actin polymerization, but less the initial reaction rates, KCTD10 might unlock an actin-capping function of EPS8 that is masked by IRSp53 (Disanza et al., 2006; Kast et al., 2014; Vaggi et al., 2011). The ternary complex failed to bundle actin filaments and even prevented actin bundling by α-actinin in *trans* (Figures 5D and 5E). Most strikingly, when we added EPS8-IRSp53-KCTD10 to bundles after these had been stabilized by α-actinin, these structures were dismantled (Figure 5E).

CUL3^{KCTD10} therefore not only displaces EPS8-IRSp53 from sites of cell contact but also terminates its ability to bundle actin filaments. Genetic experiments suggested that the latter role of CUL3^{KCTD10} is also critical for cell fusion: if CUL3^{KCTD10} restricted actin-bundling by EPS8-IRSp53, then KCTD10-depleted cells expressing a bundling deficient variant, EPS8^{RAFA}, should be able to fuse—this was the case (Figure S5C). Conversely, a variant that is more efficient in actin bundling, EPS8^{SATA} (Menna et al., 2009), prevented cell fusion even in the presence of KCTD10 (Figures 5F and S5D). We conclude that CUL3^{KCTD10} possesses dual ability in reversing localization and function of EPS8-IRSp53, thereby establishing a toggle switch for actin bundling that drives regulated cytoskeletal rearrangements needed for cell fusion.

Cortical actin bundles promote cell apposition

Next, we wished to characterize actin structures under control of CUL3^{KCTD10}, using transmission electron microscopy of differentiating C2C12 cells that were depleted KCTD10 to prolong EPS8-IRSp53 activity. KCTD10-depleted cells accumulated prominent linear actin bundles below the plasma membrane, specifically at sites of cell contact (Figures 6A and 6B); these cables were distinctive structures reminiscent of transverse arcs assembled during cell migration (Burnette et al., 2011). While KCTD10-deficient cells became closely aligned with neighboring cells over large membrane areas, they did not fuse despite myoblasts directing protrusions to the receiving myotube (Figure 6B).

(I) Cell fusion of differentiating C2C12 myoblasts that expressed EPS8 or Ub-fused EPS8 and that were transfected with control siRNAs, siRNAs against KCTD10, or siRNAs against both KCTD10 and EPS8, was followed by microscopy against MyHC and Hoechst. (I) Quantification of fusion experiments in the absence or presence of Ub-EPS8. Scale bars in (A–F) and (H) are 10 μm; scale bars in (G and I) are 100 μm.

Please cite this article in press as: Rodríguez-Pérez et al., Ubiquitin-dependent remodeling of the actin cytoskeleton drives cell fusion, Developmental Cell (2021), https://doi.org/10.1016/j.devcel.2021.01.016

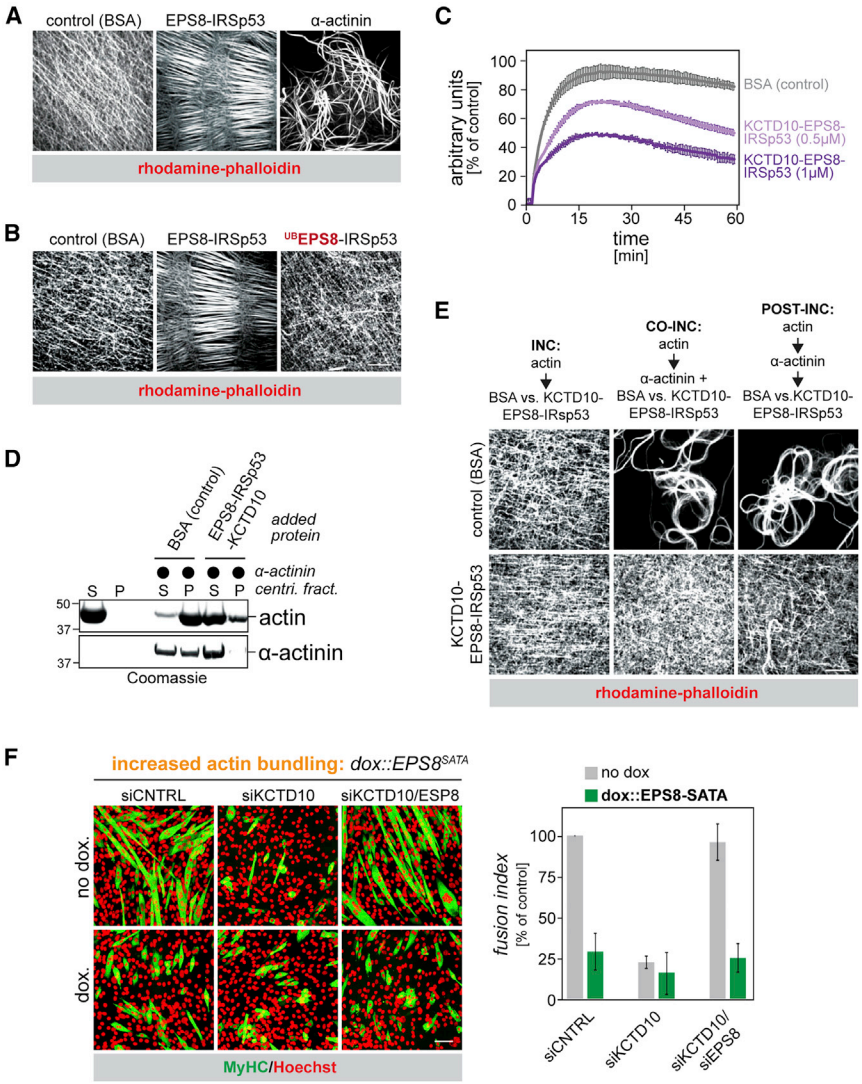

Figure 5. CUL3^{KCTD10} inhibits actin bundling

(A) Actin was polymerized in the presence of BSA, EPS8-IRSp53, or α-actinin. Actin filaments were labeled with rhodamine-phalloidin and analyzed by fluorescence microscopy (n = 3).

(B) EPS8-IRSp53 was ubiquitylated by NEDD8-modified CUL3^{KCTD10}. Actin was polymerized in the presence of BSA, EPS8-IRSp53, or ubiquitylated EPS8-IRSp53 (^{UB}EPS8-IRSp53). Actin was labeled with rhodamine-phalloidin and analyzed by fluorescence microscopy (n = 3).

(C) Actin was polymerized in the presence of BSA or increasing concentrations of KCTD10-EPS8-IRSp53.

(D) Actin was polymerized in the presence of α-actinin ± KCTD10-EPS8-IRSp53. Reactions were centrifuged and supernatant (S) and pellet (P) fractions were analyzed by western blotting.

(E) Actin was polymerized in the presence of BSA or α-actinin. *"CO-INC"*: BSA or KCTD10-EPS8-IRSp53 was added at the same time as α-actinin; *"POST-INC"*: BSA or the ternary complex was added after α-actinin had produced bundles. Actin was labeled with rhodamine-phalloidin and analyzed by fluorescence microscopy (three biological replicates).

(F) Expression of EPS8^{SATA}, a variant with higher affinity toward actin and higher bundling activity, prevents C2C12 cell fusion, as shown by MyHC and Hoechst immunofluorescence microscopy. Quantifications are shown on the right, with mean and ± SD. Scale bar is 100 μm. Scale bars in (A), (B), and (E) are 5 μm.

This is distinct from apposed control cells that readily initiated cell fusion (Figure S6). Together with our biochemical studies, these results strongly implied that CUL3^{KCTD10} limits formation of cortical actin bundles to allow cell fusion to proceed beyond membrane alignment.

To independently test whether CUL3^{KCTD10} restricts formation of cortical actin bundles, we plated myoblasts at low densities to preclude cell-cell contacts. As EPS8-IRSp53 spontaneously translocates to plasma membranes under these conditions (Figure 4A), depletion of KCTD10 might lead to increased actin bundling at stochastic sites. First, we noted that KCTD10-depleted myoblasts ceased to move, which was dependent on EPS8 and revealed that unrestricted actin bundling, likely at sites of contact with the cover slip, is deleterious for cell migration (Figure 6C). In addition, cells lacking KCTD10 formed dramatic actin structures that assembled in a circular fashion, grew upwards for hours until they extended several cell diameters above the myoblast, and then collapsed (Figures 6D and 6E). These protrusions contained EPS8 and required EPS8-IRSp53 and actin polymerization for their formation (Figure 6F), and they were prominently seen by scanning electron microscopy of KCTD10-depleted cells (Figure 6G). We conclude that CUL3^{KCTD10} restricts the EPS8-IRSp53-dependent formation of cortical actin bundles that appear to push plasma membranes outward.

Given the effects of EPS8-IRSp53 and CUL3^{KCTD10} at cell interfaces, we asked the question whether this regulatory circuit is sufficient for reversible actin bundling and membrane sculpting. We, thus, tethered EPS8 or IRSp53 to outer mitochondrial membranes and assayed for changes in the distribution or morphology of this organelle. When anchored on mitochondria, EPS8 and IRSp53 efficiently recruited KCTD10 from sites of cell contact to this organelle, which further validated the interactions described above (Figure 7A). In addition, tethered EPS8 or IRSp53 pushed organelles toward each other to establish enormous mitochondrial clusters (Figures 7B and 7C). As shown by electron microscopy, clustered mitochondria were larger in size and contained fewer cristae than those observed under control conditions, yet closely aligned their membranes with each other (Figure 7B). Organelle clustering induced by EPS8 required IRSp53 and actin polymerization and, thus, likely reflects a consequence of actin bundling in proximity of membranes (Figure 7C). EPS8 only pushed mitochondria toward each other, if CUL3^{KCTD10} was present (Figure 7C), highlighting

Please cite this article in press as: Rodríguez-Pérez et al., Ubiquitin-dependent remodeling of the actin cytoskeleton drives cell fusion, Developmental Cell (2021), https://doi.org/10.1016/j.devcel.2021.01.016

CellPress

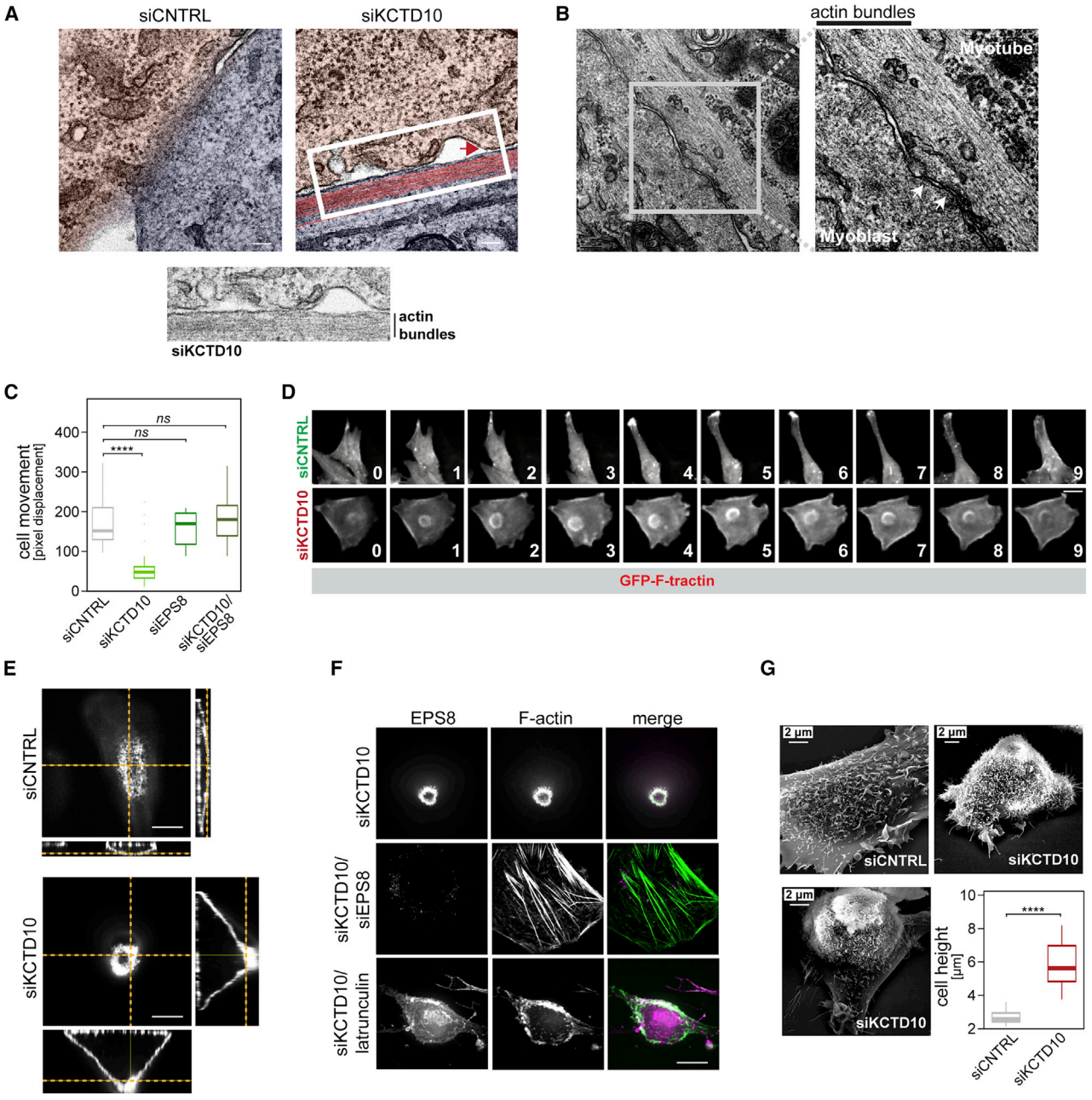

Figure 6. EPS8-IRSp53 pushes membranes outward

(A) C2C12 myoblasts were depleted of KCTD10 as indicated, induced to differentiate, and imaged by transmission electron microscopy. Actin bundles detected in KCTD10-depleted cells were false-colored (red). Scale bars, 100 nm.

(B) KCTD10-depleted myoblasts still show protrusions toward the myotube (arrows), as seen by transmission electron microscopy. Scale bar sizes are shown.

(C) Migration of C2C12 myoblasts expressing GFP-F-tractin transfected with control siRNAs or siRNAs targeting KCTD10, EPS8, or both, was followed by live cell imaging. Distance from the starting point of a cell was measured after 2 h. (****$p < 0.0001$).

(D) C2C12 myoblasts were transfected with siRNAs targeting KCTD10 and followed by live cell imaging.

(E) C2C12 myoblasts were treated with control siRNAs or siRNAs targeting KCTD10 and analyzed for their actin cytoskeleton using rhodamine-phalloidin by confocal fluorescence microscopy.

(F) C2C12 myoblasts were depleted of KCTD10 or KCTD10 and EPS8. Alternatively, KCTD10-depleted cells were treated with latrunculin. Actin was stained with rhodamine phalloidin and analyzed by fluorescence microscopy.

(G) C2C12 myoblasts were treated with control siRNAs or siRNAs against KCTD10 and imaged by scanning electron microscopy. Cell height was quantified as shown to the right. Scale bars in (D and E) are 10 µm. (****$p < 0.0001$).

Please cite this article in press as: Rodríguez-Pérez et al., Ubiquitin-dependent remodeling of the actin cytoskeleton drives cell fusion, Developmental Cell (2021), https://doi.org/10.1016/j.devcel.2021.01.016

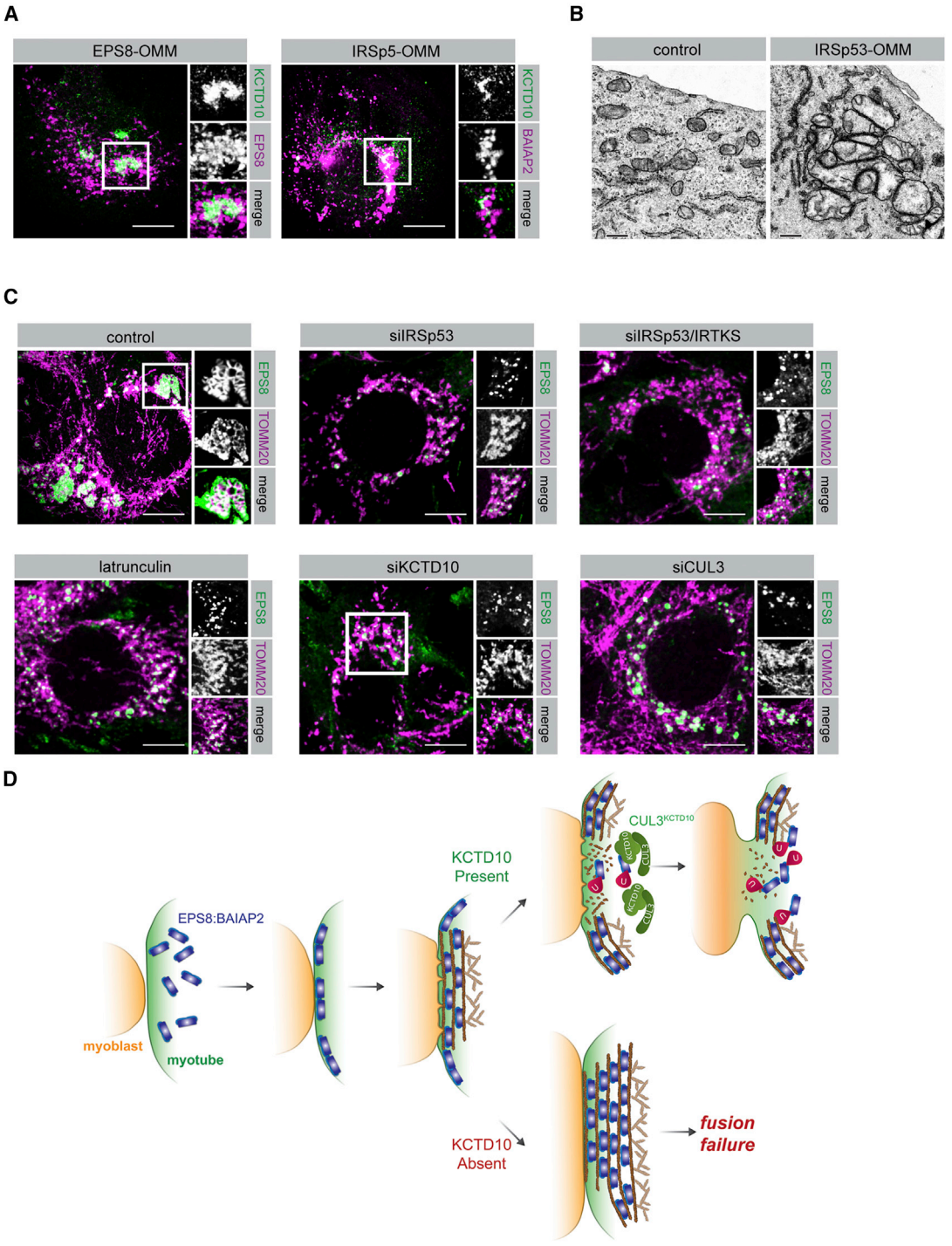

Figure 7. EPS8-IRSp53 acts independently of membrane identity

(A) EPS8 and IRSp53 were anchored to the mitochondrial outer membrane through the transmembrane domain of OMP25, and EPS8, IRSp53, and KCTD10 localization was monitored by immunofluorescence microscopy.

(B) Mitochondrial tethering of IRSp53 causes large organellar clusters, as seen by transmission electron microscopy.

(C) Mitochondrial tethering of EPS8 triggers organellar clustering dependent on IRSp53, $CUL3^{KCTD10}$ (siRNA depletion), and actin polymerization (latrunculin treatment). Mitochondrial clustering was analyzed by localizing EPS8-OMM fusions and the mitochondrial protein TOMM20 through immunofluorescence microscopy.

(D) Model of reversible actin bundling by EPS8-IRSp53 driving cell fusion. Scale bars for immunofluorescence are 5 μm; scale bars for EM images are shown.

Please cite this article in press as: Rodríguez-Pérez et al., Ubiquitin-dependent remodeling of the actin cytoskeleton drives cell fusion, Developmental Cell (2021), https://doi.org/10.1016/j.devcel.2021.01.016

that ubiquitylation drives cytoskeletal and membrane rearrangements. These observations strongly suggest that actin bundling by EPS8-IRSp53 helps push neighboring cells toward each other for membrane apposition. By re-localizing and inhibiting EPS8-IRSp53, monoubiquitylation by CUL3^{KCTD10} restricts actin bundling at cell interfaces and allows the fusion program to proceed beyond the apposition stage. Actin bundling is, therefore, precisely controlled by a ubiquitin-dependent toggle switch to allow successful cell fusion and development.

DISCUSSION

The actin cytoskeleton provides a force for the remodeling of plasma membranes that drives cell migration, communication, and fusion. A complex program, such as cell fusion, not only depends on efficient filament formation or bundling but also requires coordinated transitions from one actin structure into another. How dynamic regulation of the actin cytoskeleton is accomplished with temporal and spatial precision is not completely understood.

Addressing this gap, we identified CUL3^{KCTD10} as a regulator of reversible actin bundling at sites of cell-cell contact and showed that it is required for cell fusion to proceed beyond cell apposition (Figure 7D). While we performed our work in C2C12 myoblasts, *KCTD10* deletion in mice or zebrafish interfered with angiogenesis and heart formation (Hu et al., 2014; Ren et al., 2014), two processes that occur before most skeletal muscle is formed (Papizan et al., 2018). However, recent work found that zebrafish heart development involves transient cardiomyocyte fusion (Sawamiphak et al., 2017). Moreover, tissue-specific deletion of *CUL3* interfered with myoblast fusion in mice (Blondelle et al., 2019; Papizan et al., 2018), indicating that the regulatory circuit reported here plays critical roles for cell fusion in organisms as well.

CUL3^{KCTD10} controls cell fusion by monoubiquitylating EPS8, a protein that is part of two complexes: when bound to ABI1, EPS8 caps barbed ends of actin filaments and impairs actin polymerization (Disanza et al., 2004; Hertzog et al., 2010), yet when associated with IRSp53 or IRTKS, EPS8 crosslinks and stabilizes the same structures (Disanza et al., 2006). CUL3^{KCTD10} targets the EPS8-IRSp53 complex and specifically impacts actin bundling. Although not critical for cell fusion, CUL3^{KCTD10} also monoubiquitylates α-actinin. Similar to EPS8-IRSp53, α-actinin bundles actin filaments and its dysregulation can impede myoblast fusion (Blondelle et al., 2019). Befitting their shared regulation by CUL3^{KCTD10}, we found that EPS8 and α-actinin together shape the actin cytoskeleton during cell fusion. As synergy between bundlers can increase the force exerted by crosslinked filaments (Mogilner and Rubinstein, 2005), the collaboration between EPS8-IRSp53 and α-actinin might allow cells to overcome the repulsion exerted by the hydrated and charged lipid head groups of approaching plasma membranes during membrane apposition. In addition, EPS8-IRSp53 and α-actinin likely stabilize the cortical actomyosin network in myotubes to provide mechanical resistance critical for cell fusion (Kim et al., 2015).

Monoubiquitylation by CUL3^{KCTD10} displaced EPS8-IRSp53 from sites of cell contact and restricted the bundling activity of this complex (Figure 7D). The complex between KCTD10, EPS8, and IRSp53 also dismantled actin bundles that were stabilized by α-actinin. In this manner, CUL3^{KCTD10} generates a toggle switch to terminate actin bundling when it is no longer required and thus prevent unnecessary stiffening of the actomyosin network. KCTD10 bound the split-PH domains of EPS8, and CUL3^{KCTD10} modified at least one Lys residue in this region. PH domains recognize phosphoinositide lipids, such as PI(4,5)P2, that are known to be required for cell fusion (Bothe et al., 2014). Binding to KCTD10 or addition of the bulky and charged ubiquitin to a PH-domain might interfere with PI(4,5)P2 binding and impair membrane targeting of EPS8. In a similar manner, the association of KCTD10 with the IMD-domain of IRSp53 might prevent actin binding of the latter protein. How the KCTD10-EPS8-IRSp53 complex dismantles actin bundles is unknown and could occur by severing, displacement of α-actinin, or changes in protein interactions at the interface of actin filaments. Irrespective of the mechanism, our work shows that actin bundling is regulated by a specific posttranslational modification, i.e., monoubiquitylation.

Loss of CUL3^{KCTD10} allowed us to visualize the actin bundles produced by EPS8-IRSp53, even though these cables likely exist for a short time during cell fusion. We found that bundles stabilized by EPS8-IRSp53 formed at sites of cell contact and ran in parallel to the plasma membrane. The arrangement of EPS8-IRSp53-dependent bundles at cell interfaces resembled transverse arcs that form behind lamellipodia of mobile cells or peripheral actomyosin bundles that establish cell barriers or E-cadherin-dependent cell adhesions (Burnette et al., 2011; Heuzé et al., 2019; Rajakylä et al., 2020). Transverse arcs are stabilized by α-actinin and provide a scaffold for branched actin networks to push lamellipodial membranes forward (Dolat et al., 2014). We hypothesize that actin bundles produced by EPS8-IRSp53 also support formation of branched actin networks that promote membrane apposition (Dhanyasi et al., 2015; Duan et al., 2018; Kim et al., 2015; Zhang et al., 2020) and likely strengthen the mechanical resistance of the actomyosin network in receiving cells (Kim et al., 2015). Transverse arcs are dynamic and need to be turned over for cell migration, just as CUL3^{KCTD10}-dependent disassembly of cortical actin cables allows fusion to proceed beyond membrane apposition. However, assembly of transverse arcs requires their binding to focal adhesions (Burnette et al., 2011), yet we observed EPS8-IRSp53-dependent actin structures in KCTD10-depleted myoblasts devoid of cell-cell contacts. How these dramatic protrusions form in the absence of focal adhesion is unclear and will require further investigation.

Our discovery of a ubiquitin-dependent toggle switch for actin bundling reveals tight spatiotemporal control of cytoskeletal rearrangements during cell fusion. We predict that other structures, such as the actin focus in myoblasts or filopodial protrusions, will also be restricted by effectors that trigger disassembly of actin bundles or networks in response to specific cellular cues. The treadmilling of transverse arcs in migrating cells or the dynamic nature of filopodia in dendrites implies that such switches also play critical roles beyond cell fusion (Burnette et al., 2011; Gallop, 2020). Identifying negative regulators of the actin cytoskeleton will provide more insight into cytoskeletal rearrangements during development, and it could offer a route to rescuing cell fusion under pathological conditions to provide

therapeutic benefit for patients of muscle or bone diseases that are currently difficult to treat.

STAR★METHODS

Detailed methods are provided in the online version of this paper and include the following:

- KEY RESOURCES TABLE
- RESOURCE AVAILABILITY
  - Lead Contact
  - Materials Availability
  - Data and Code Availability
- EXPERIMENTAL MODEL AND SUBJECT DETAILS
- METHODS DETAILS
  - Antibodies
  - Individual siRNA sequences
  - Cloning
  - R_{MHC} index analysis
  - Fusion index analysis
  - High content screening and myotube analysis
  - Cell culture
  - Viral production
  - Lentiviral spinfections
  - Whole cell lysates
  - *In vitro* ubiquitylation
  - *In vitro* binding
  - Immunofluorescence and confocal microscopy
  - Myogenesis functional assays
  - Live cell imaging
  - Cell mixing assays
  - Cell and particle tracking
  - Protein purifications
  - Actin polymerization and bundling assays
  - Immunoprecipitation and mass spectrometry
  - Genome editing
  - NGS Library Prep and RNA-seq
  - RNA-seq Alignment and Expression Analysis
  - Transmission and scanning electron microscopy
- QUANTIFICATION AND STATISTICAL ANALYSIS

SUPPLEMENTAL INFORMATION

Supplemental Information can be found online at https://doi.org/10.1016/j.devcel.2021.01.016.

ACKNOWLEDGMENTS

We are grateful to Henry Ho, Andres Lebenson, Matt Welch, Achim Werner, and Eugene Oh for suggestions and comments on the manuscript. We thank all members of our laboratory for continuous discussions and support. We thank the Welch and Zoncu labs at University of California (UC) Berkeley for gifts of important reagents. Thank you to the staff at the UC Berkeley Electron Microscope Laboratory, especially Reena Zalpuri and Guangwei Min, for advice and assistance in electron microscopy sample preparation and data collection. We thank Dr. Mary West and Dr. Pingping He of the High-Throughput Screening Facility (HTSF) at UC Berkeley, which provided instrumentation funded by NIH award S10OD021828. This work used the Vincent J. Coates Genomics Sequencing Laboratory at UC Berkeley, supported by NIH S10 OD018174, and the Vincent J. Coates Proteomics/Mass Spectrometry Laboratory at UC Berkeley, supported in part by NIH award S10 Instrumentation grant S10RR025622. F.R.-P. is a Howard Hughes Medical Institute Gilliam Fellow. A.G.M. was supported by a postdoctoral fellowship, PF-15-215-01 – DCC from the American Cancer Society. A.J.I. is a recipient of a National Science Foundation pre-doctoral fellowship. M.R. is an Investigator of the Howard Hughes Medical Institute.

AUTHOR CONTRIBUTIONS

Conceptualization, F.R.-P., A.G.M., and M.R.; methodology, F.R.-P., A.G.M., A.P., A.J.I., B.G.-M., and M.R.; investigation: F.R.-P., A.G.M., A.P., A.J.I., and B.G.-M.; writing–original draft, F.R.P., A.G.M., and M.R.; writing–reviewing & editing, all authors; funding acquisition, F.R.-P., A.G.M., A.J.I., and M.R.; supervision, M.R.

DECLARATION OF INTERESTS

M.R. is a co-founder and consultant to Nurix Therapeutics, a publicly traded company in the ubiquitin space. M.R. is a member of the scientific advisory board of Monte Rosa Therapeutics.

Received: June 16, 2020
Revised: November 14, 2020
Accepted: January 24, 2021
Published: February 19, 2021

REFERENCES

Bennett, E.J., Rush, J., Gygi, S.P., and Harper, J.W. (2010). Dynamics of cullin-RING ubiquitin ligase network revealed by systematic quantitative proteomics. Cell *143*, 951–965.

Bi, P., Ramirez-Martinez, A., Li, H., Cannavino, J., McAnally, J.R., Shelton, J.M., Sánchez-Ortiz, E., Bassel-Duby, R., and Olson, E.N. (2017). Control of muscle formation by the fusogenic micropeptide myomixer. Science *356*, 323–327.

Blondelle, J., Tallapaka, K., Seto, J.T., Ghassemian, M., Clark, M., Laitila, J.M., Bournazos, A., Singer, J.D., and Lange, S. (2019). Cullin-3 dependent deregulation of ACTN1 represents a new pathogenic mechanism in nemaline myopathy. JCI Insight *5*, e125665.

Bothe, I., Deng, S., and Baylies, M. (2014). PI(4,5)P2 regulates myoblast fusion through Arp2/3 regulator localization at the fusion site. Development *141*, 2289–2301.

Bray, N.L., Pimentel, H., Melsted, P., and Pachter, L. (2016). Near-optimal probabilistic RNA-seq quantification. Nat. Biotechnol. *34*, 525–527.

Brukman, N.G., Uygur, B., Podbilewicz, B., and Chernomordik, L.V. (2019). How cells fuse. J. Cell Biol. *218*, 1436–1451.

Burnette, D.T., Manley, S., Sengupta, P., Sougrat, R., Davidson, M.W., Kachar, B., and Lippincott-Schwartz, J. (2011). A role for actin arcs in the leading-edge advance of migrating cells. Nat. Cell Biol. *13*, 371–381.

Deng, S., Azevedo, M., and Baylies, M. (2017). Acting on identity: myoblast fusion and the formation of the syncytial muscle fiber. Semin. Cell Dev. Biol. *72*, 45–55.

Deng, S., Bothe, I., and Baylies, M. (2016). Diaphanous regulates SCAR complex localization during Drosophila myoblast fusion. Fly (Austin) *10*, 178–186.

Deng, S., Bothe, I., and Baylies, M.K. (2015). The formin diaphanous regulates myoblast fusion through actin polymerization and Arp2/3 regulation. PLoS Genet. *11*, e1005381.

DeWitt, M.A., Corn, J.E., and Carroll, D. (2017). Genome editing via delivery of Cas9 ribonucleoprotein. Methods *121–122*, 9–15.

Dhanyasi, N., Segal, D., Shimoni, E., Shinder, V., Shilo, B.Z., VijayRaghavan, K., and Schejter, E.D. (2015). Surface apposition and multiple cell contacts promote myoblast fusion in Drosophila flight muscles. J. Cell Biol. *211*, 191–203.

Di Gioia, S.A., Connors, S., Matsunami, N., Cannavino, J., Rose, M.F., Gilette, N.M., Artoni, P., de Macena Sobreira, N.L., Chan, W.M., Webb, B.D., et al. (2017). A defect in myoblast fusion underlies Carey-Fineman-Ziter syndrome. Nat. Commun. *8*, 16077.

Disanza, A., Carlier, M.F., Stradal, T.E., Didry, D., Frittoli, E., Confalonieri, S., Croce, A., Wehland, J., Di Fiore, P.P., and Scita, G. (2004). Eps8 controls actin-based motility by capping the barbed ends of actin filaments. Nat. Cell Biol. *6*, 1180–1188.

Disanza, A., Mantoani, S., Hertzog, M., Gerboth, S., Frittoli, E., Steffen, A., Berhoerster, K., Kreienkamp, H.J., Milanesi, F., Di Fiore, P.P., et al. (2006). Regulation of cell shape by Cdc42 is mediated by the synergic actin-bundling activity of the Eps8-IRSp53 complex. Nat. Cell Biol. *8*, 1337–1347.

Doherty, J.T., Lenhart, K.C., Cameron, M.V., Mack, C.P., Conlon, F.L., and Taylor, J.M. (2011). Skeletal muscle differentiation and fusion are regulated by the BAR-containing Rho-GTPase-activating protein (Rho-GAP), GRAF1. J. Biol. Chem. *286*, 25903–25921.

Dolat, L., Hunyara, J.L., Bowen, J.R., Karasmanis, E.P., Elgawly, M., Galkin, V.E., and Spiliotis, E.T. (2014). Septins promote stress fiber-mediated maturation of focal adhesions and renal epithelial motility. J. Cell Biol. *207*, 225–235.

Duan, R., Kim, J.H., Shilagardi, K., Schiffhauer, E.S., Lee, D.M., Son, S., Li, S., Thomas, C., Luo, T., Fletcher, D.A., et al. (2018). Spectrin is a mechanoresponsive protein shaping fusogenic synapse architecture during myoblast fusion. Nat. Cell Biol. *20*, 688–698.

Funato, Y., Terabayashi, T., Suenaga, N., Seiki, M., Takenawa, T., and Miki, H. (2004). IRSp53/Eps8 complex is important for positive regulation of Rac and cancer cell motility/invasiveness. Cancer Res. *64*, 5237–5244.

Galletta, B.J., Chakravarti, M., Banerjee, R., and Abmayr, S.M. (2004). SNS: adhesive properties, localization requirements and ectodomain dependence in S2 cells and embryonic myoblasts. Mech. Dev. *121*, 1455–1468.

Gallop, J.L. (2020). Filopodia and their links with membrane traffic and cell adhesion. Semin. Cell Dev. Biol. *102*, 81–89.

Geisbrecht, E.R., Haralalka, S., Swanson, S.K., Florens, L., Washburn, M.P., and Abmayr, S.M. (2008). Drosophila ELMO/CED-12 interacts with Myoblast city to direct myoblast fusion and ommatidial organization. Dev. Biol. *314*, 137–149.

Gupta, V.A., and Beggs, A.H. (2014). Kelch proteins: emerging roles in skeletal muscle development and diseases. Skelet. Muscle *4*, 11.

Haralalka, S., Shelton, C., Cartwright, H.N., Guo, F., Trimble, R., Kumar, R.P., and Abmayr, S.M. (2014). Live imaging provides new insights on dynamic F-actin filopodia and differential endocytosis during myoblast fusion in Drosophila. PLoS One *9*, e114126.

Hertzog, M., Milanesi, F., Hazelwood, L., Disanza, A., Liu, H., Perlade, E., Malabarba, M.G., Pasqualato, S., Maiolica, A., Confalonieri, S., et al. (2010). Molecular basis for the dual function of Eps8 on actin dynamics: bundling and capping. PLoS Biol. *8*, e1000387.

Heuzé, M.L., Sankara Narayana, G.H.N., D'Alessandro, J., Cellerin, V., Dang, T., Williams, D.S., Van Hest, J.C., Marcq, P., Mège, R.M., and Ladoux, B. (2019). Myosin II isoforms play distinct roles in adherens junction biogenesis. eLife *8*, e46599.

Hu, X., Gan, S., Xie, G., Li, L., Chen, C., Ding, X., Han, M., Xiang, S., and Zhang, J. (2014). KCTD10 is critical for heart and blood vessel development of zebrafish. Acta Biochim. Biophys. Sin. (Shanghai) *46*, 377–386.

Huttlin, E.L., Ting, L., Bruckner, R.J., Gebreab, F., Gygi, M.P., Szpyt, J., Tam, S., Zarraga, G., Colby, G., Baltier, K., et al. (2015). The BioPlex network: a systematic exploration of the human interactome. Cell *162*, 425–440.

Jin, L., Pahuja, K.B., Wickliffe, K.E., Gorur, A., Baumgärtel, C., Schekman, R., and Rape, M. (2012). Ubiquitin-dependent regulation of COPII coat size and function. Nature *482*, 495–500.

Kast, D.J., Yang, C., Disanza, A., Boczkowska, M., Madasu, Y., Scita, G., Svitkina, T., and Dominguez, R. (2014). Mechanism of IRSp53 inhibition and combinatorial activation by Cdc42 and downstream effectors. Nat. Struct. Mol. Biol. *21*, 413–422.

Kim, J.H., and Chen, E.H. (2019). The fusogenic synapse at a glance. J. Cell Sci. *132*, jcs213124.

Kim, J.H., Ren, Y., Ng, W.P., Li, S., Son, S., Kee, Y.S., Zhang, S., Zhang, G., Fletcher, D.A., Robinson, D.N., and Chen, E.H. (2015). Mechanical tension drives cell membrane fusion. Dev. Cell *32*, 561–573.

Kim, S., Shilagardi, K., Zhang, S., Hong, S.N., Sens, K.L., Bo, J., Gonzalez, G.A., and Chen, E.H. (2007). A critical function for the actin cytoskeleton in targeted exocytosis of prefusion vesicles during myoblast fusion. Dev. Cell *12*, 571–586.

Krugmann, S., Jordens, I., Gevaert, K., Driessens, M., Vandekerckhove, J., and Hall, A. (2001). Cdc42 induces filopodia by promoting the formation of an IRSp53:Mena complex. Curr. Biol. *11*, 1645–1655.

Lee, D.M., and Chen, E.H. (2019). Drosophila myoblast fusion: invasion and resistance for the ultimate union. Annu. Rev. Genet. *53*, 67–91.

Lehka, L., and Rędowicz, M.J. (2020). Mechanisms regulating myoblast fusion: a multilevel interplay. Semin. Cell Dev. Biol. *104*, 81–92.

Manford, A.G., Rodríguez-Pérez, F., Shih, K.Y., Shi, Z., Berdan, C.A., Choe, M., Titov, D.V., Nomura, D.K., and Rape, M. (2020). A cellular mechanism to detect and alleviate reductive stress. Cell *183*, 46–61.e21.

Mark, K.G., Loveless, T.B., and Toczyski, D.P. (2016). Isolation of ubiquitinated substrates by tandem affinity purification of E3 ligase-polyubiquitin-binding domain fusions (ligase traps). Nat. Protoc. *11*, 291–301.

Massarwa, R., Carmon, S., Shilo, B.Z., and Schejter, E.D. (2007). WIP/WASp-based actin-polymerization machinery is essential for myoblast fusion in Drosophila. Dev. Cell *12*, 557–569.

McGourty, C.A., Akopian, D., Walsh, C., Gorur, A., Werner, A., Schekman, R., Bautista, D., and Rape, M. (2016). Regulation of the CUL3 ubiquitin ligase by a calcium-dependent co-adaptor. Cell *167*, 525–538.e14.

Meerbrey, K.L., Hu, G., Kessler, J.D., Roarty, K., Li, M.Z., Fang, J.E., Herschkowitz, J.I., Burrows, A.E., Ciccia, A., Sun, T., et al. (2011). The pINDUCER lentiviral toolkit for inducible RNA interference in vitro and in vivo. Proc. Natl. Acad. Sci. USA *108*, 3665–3670.

Mena, E.L., Kjolby, R.A.S., Saxton, R.A., Werner, A., Lew, B.G., Boyle, J.M., Harland, R., and Rape, M. (2018). Dimerization quality control ensures neuronal development and survival. Science *362*, eaap8236.

Menna, E., Disanza, A., Cagnoli, C., Schenk, U., Gelsomino, G., Frittoli, E., Hertzog, M., Offenhauser, N., Sawallisch, C., Kreienkamp, H.J., et al. (2009). Eps8 regulates axonal filopodia in hippocampal neurons in response to brain-derived neurotrophic factor (BDNF). PLoS Biol. *7*, e1000138.

Millay, D.P., O'Rourke, J.R., Sutherland, L.B., Bezprozvannaya, S., Shelton, J.M., Bassel-Duby, R., and Olson, E.N. (2013). Myomaker is a membrane activator of myoblast fusion and muscle formation. Nature *499*, 301–305.

Mogilner, A., and Rubinstein, B. (2005). The physics of filopodial protrusion. Biophys. J. *89*, 782–795.

Oh, E., Akopian, D., and Rape, M. (2018). Principles of ubiquitin-dependent signaling. Annu. Rev. Cell Dev. Biol. *34*, 137–162.

Oh, E., Mark, K.G., Mocciaro, A., Watson, E.R., Prabu, J.R., Cha, D.D., Kampmann, M., Gamarra, N., Zhou, C.Y., and Rape, M. (2020). Gene expression and cell identity controlled by anaphase-promoting complex. Nature *579*, 136–140.

Özkan, E., Chia, P.H., Wang, R.R., Goriatcheva, N., Borek, D., Otwinowski, Z., Walz, T., Shen, K., and Garcia, K.C. (2014). Extracellular architecture of the SYG-1/SYG-2 adhesion complex instructs synaptogenesis. Cell *156*, 482–494.

Papizan, J.B., Vidal, A.H., Bezprozvannaya, S., Bassel-Duby, R., and Olson, E.N. (2018). Cullin-3-RING ubiquitin ligase activity is required for striated muscle function in mice. J. Biol. Chem. *293*, 8802–8811.

Pereira, M., Petretto, E., Gordon, S., Bassett, J.H.D., Williams, G.R., and Behmoaras, J. (2018). Common signalling pathways in macrophage and osteoclast multinucleation. J. Cell Sci. *131*, jcs216267.

Petrany, M.J., and Millay, D.P. (2019). Cell fusion: merging membranes and making muscle. Trends Cell Biol *29*, 964–973.

Piccinini, F., Kiss, A., and Horvath, P. (2016). CellTracker (not only) for dummies. Bioinformatics *32*, 955–957.

Pimentel, H., Bray, N.L., Puente, S., Melsted, P., and Pachter, L. (2017). Differential analysis of RNA-seq incorporating quantification uncertainty. Nat. Methods *14*, 687–690.

Pinkas, D.M., Sanvitale, C.E., Bufton, J.C., Sorrell, F.J., Solcan, N., Chalk, R., Doutch, J., and Bullock, A.N. (2017). Structural complexity in the KCTD family of Cullin3-dependent E3 ubiquitin ligases. Biochem. J. *474*, 3747–3761.

Quinn, M.E., Goh, Q., Kurosaka, M., Gamage, D.G., Petrany, M.J., Prasad, V., and Millay, D.P. (2017). Myomerger induces fusion of non-fusogenic cells and is required for skeletal muscle development. Nat. Commun. *8*, 15665.

Rajakylä, E.K., Lehtimäki, J.I., Acheva, A., Schaible, N., Lappalainen, P., Krishnan, R., and Tojkander, S. (2020). Assembly of peripheral actomyosin bundles in epithelial cells is dependent on the CaMKK2/AMPK pathway. Cell Rep *30*, 4266–4280.e4.

Rape, M. (2018). Ubiquitylation at the crossroads of development and disease. Nat. Rev. Mol. Cell Biol. *19*, 59–70.

Ren, K., Yuan, J., Yang, M., Gao, X., Ding, X., Zhou, J., Hu, X., Cao, J., Deng, X., Xiang, S., and Zhang, J. (2014). KCTD10 is involved in the cardiovascular system and Notch signaling during early embryonic development. PLoS One *9*, e112275.

Ribeiro, Ede A., Pinotsis, N., Ghisleni, A., Salmazo, A., Konarev, P.V., Kostan, J., Sjöblom, B., Schreiner, C., Polyansky, A.A., Gkougkoulia, E.A., et al. (2014). The structure and regulation of human muscle alpha-actinin. Cell *159*, 1447–1460.

Richardson, B.E., Beckett, K., Nowak, S.J., and Baylies, M.K. (2007). SCAR/WAVE and Arp2/3 are crucial for cytoskeletal remodeling at the site of myoblast fusion. Development *134*, 4357–4367.

Rosen, G.D., Sanes, J.R., LaChance, R., Cunningham, J.M., Roman, J., and Dean, D.C. (1992). Roles for the integrin VLA-4 and its counter receptor VCAM-1 in myogenesis. Cell *69*, 1107–1119.

Ruiz-Gómez, M., Coutts, N., Price, A., Taylor, M.V., and Bate, M. (2000). Drosophila dumbfounded: a myoblast attractant essential for fusion. Cell *102*, 189–198.

Sawamiphak, S., Kontarakis, Z., Filosa, A., Reischauer, S., and Stainier, D.Y.R. (2017). Transient cardiomyocyte fusion regulates cardiac development in zebrafish. Nat. Commun. *8*, 1525.

Sbalzarini, I.F., and Koumoutsakos, P. (2005). Feature point tracking and trajectory analysis for video imaging in cell biology. J. Struct. Biol. *151*, 182–195.

Schäfer, G., Weber, S., Holz, A., Bogdan, S., Schumacher, S., Müller, A., Renkawitz-Pohl, R., and Onel, S.F. (2007). The Wiskott-Aldrich syndrome protein (WASP) is essential for myoblast fusion in Drosophila. Dev. Biol. *304*, 664–674.

Schindelin, J., Arganda-Carreras, I., Frise, E., Kaynig, V., Longair, M., Pietzsch, T., Preibisch, S., Rueden, C., Saalfeld, S., Schmid, B., et al. (2012). Fiji: an open-source platform for biological-image analysis. Nat. Methods *9*, 676–682.

Segal, D., Dhanyasi, N., Schejter, E.D., and Shilo, B.Z. (2016). Adhesion and fusion of muscle cells are promoted by filopodia. Dev. Cell *38*, 291–304.

Sens, K.L., Zhang, S., Jin, P., Duan, R., Zhang, G., Luo, F., Parachini, L., and Chen, E.H. (2010). An invasive podosome-like structure promotes fusion pore formation during myoblast fusion. J. Cell Biol. *191*, 1013–1027.

Tong, K.I., Kobayashi, A., Katsuoka, F., and Yamamoto, M. (2006). Two-site substrate recognition model for the Keap1-Nrf2 system: a hinge and latch mechanism. Biol. Chem. *387*, 1311–1320.

Vaggi, F., Disanza, A., Milanesi, F., Di Fiore, P.P., Menna, E., Matteoli, M., Gov, N.S., Scita, G., and Ciliberto, A. (2011). The Eps8/IRSp53/VASP network differentially controls actin capping and bundling in filopodia formation. PLoS Comput. Biol. *7*, e1002088.

Werner, A., Baur, R., Kaya, D., Teerikorpi, N., and Rape, M. (2018). Multivalent substrate recognition by an E3 ligase is essential for neural crest specification. eLife *7*, e35407.

Werner, A., Iwasaki, S., McGourty, C.A., Medina-Ruiz, S., Teerikorpi, N., Fedrigo, I., Ingolia, N.T., and Rape, M. (2015). Cell-fate determination by ubiquitin-dependent regulation of translation. Nature *525*, 523–527.

Wickliffe, K.E., Lorenz, S., Wemmer, D.E., Kuriyan, J., and Rape, M. (2011). The mechanism of linkage-specific ubiquitin chain elongation by a single-subunit e2. Cell *144*, 769–781.

Yu, M., Zhao, H., Chen, T., Tian, Y., Li, M., Wu, K., Bian, Y., Su, S., Cao, Y., Ning, Y., et al. (2018). Mutational analysis of IZUMO1R in women with fertilization failure and polyspermy after in vitro fertilization. J. Assist. Reprod. Genet. *35*, 539–544.

Zhang, Q., Vashisht, A.A., O'Rourke, J., Corbel, S.Y., Moran, R., Romero, A., Miraglia, L., Zhang, J., Durrant, E., Schmedt, C., et al. (2017). The microprotein Minion controls cell fusion and muscle formation. Nat. Commun. *8*, 15664.

Zhang, R., Lee, D.M., Jimah, J.R., Gerassimov, N., Yang, C., Kim, S., Luvsanjav, D., Winkelman, J., Mettlen, M., Abrams, M.E., et al. (2020). Dynamin regulates the dynamics and mechanical strength of the actin cytoskeleton as a multifilament actin-bundling protein. Nat. Cell Biol. *22*, 674–688.

Zhuang, M., Calabrese, M.F., Liu, J., Waddell, M.B., Nourse, A., Hammel, M., Miller, D.J., Walden, H., Duda, D.M., Seyedin, S.N., et al. (2009). Structures of SPOP-substrate complexes: insights into molecular architectures of BTB-Cul3 ubiquitin ligases. Mol. Cell *36*, 39–50.

Please cite this article in press as: Rodríguez-Pérez et al., Ubiquitin-dependent remodeling of the actin cytoskeleton drives cell fusion, Developmental Cell (2021), https://doi.org/10.1016/j.devcel.2021.01.016

CellPress

STAR★METHODS

KEY RESOURCES TABLE

REAGENT or RESOURCE	SOURCE	IDENTIFIER
Antibodies		
Rabbit monoclonal α-HA-TAG	Cell Signaling Technologies	Cat# 3724; Clone C29F4; RRID:AB_1549585
Mouse monoclonal α-FLAG	Sigma-Aldrich	Cat# F1804; Clone M2; RRID:AB_262044
Rabbit monoclonal α-CUL3	Bethyl Laboratories	Cat# A301-109A; RRID:AB_873023
Rabbit α-KCTD10	Atlas Antibodies	Cat# HPA014273; RRID:AB_1852159
Mouse monoclonal α-Myosin heavy chain, sarcomere (MHC)	Developmental Studies Hybridoma Bank (DHSB)	Clone MF20; RRID:AB_1293549
Mouse monoclonal α-Myogenin	Developmental Studies Hybridoma Bank (DHSB)	Clone 5FD; RRID:AB_2146602
Rat monoclonal α-LAMP1	Developmental Studies Hybridoma Bank (DHSB)	Clone 1D4B; RRID:AB_2134500
Mouse monoclonal anti-β-ACTIN	MP Biomedicals	Cat# 08691001; Clone C4; RRID:AB_2335304
Rabbit α-DYKDDDDK Tag	Cell Signaling Technologies	Cat# 2368; RRID:AB_2217020
Rabbit α-IRSp53 (BAIAP2)	Atlas Antibodies	Cat# HPA023310; RRID:AB_1845264
Rabbit α-TOMM20	Atlas Antibodies	Cat# HPA01156; RRID:AB_1080326
Rabbit α-IRTKS (BAIAP2L1)	Atlas Antibodies	Cat# HPA021257; RRID:AB_1845266
Rabbit monoclonal α-VINCULIN	Cell Signalin Technologies	Cat# 13901; Clone E1E9V; RRID:AB_2728768
Mouse monoclonal α-EPS8	BD Transduction Labs	Cat# 610143; Clone 15; RRID:AB_397544
Sheep α-ESGP (MYMX)	R&D Systems	Cat# AF4580; RRID:AB_952042
Mouse monoclonal α-Sarcomeric α-actinin	Sigma-Aldrich	Cat# A7811; Clone EA-53; RRID:AB_476766
Goat Alexa Fluor Plus 488 anti mouse	Thermo Fisher Scientific	Cat# A32723
Goat Alexa Fluor Plus 488 anti rabbit	Thermo Fisher Scientific	Cat# A32731
Goat Alexa Fluor Plus 647 anti mouse	Thermo Fisher Scientific	Cat# A32728
Goat Alexa Fluor Plus 647 anti rabbit	Thermo Fisher Scientific	Cat# A32733
Normal Mouse IgG	Santa Cruz Biotechnology, Inc.	Cat# sc-2025; RRID:AB_737182
ANTI-FLAG® M2 Affinity Agarose Gel slurry	Sigma-Aldrich	Cat# A2220
Bacterial and Virus Strains		
E. coli LOBSTER Cells	Kerafast	EC1002
E. coli: One Shot Stbl3 Chemically competent cells	Thermo Fisher Scientific	Cat#C737303
Chemicals, Peptides, and Recombinant Proteins		
mCherry-Cas9^{NLS}	UC Berkeley QB3 MacroLab	N/A
$^{GST\text{-}TEV}$Cul3-RBX1	This Paper	N/A
^{MBP}EPS8^{FLAG}	This Paper	N/A
^{MBP}IRSp54:EPS8^{FLAG}	This Paper	N/A
$^{MBP\text{-}His}$KCTD10	This Paper	N/A
^{MBP}IRSp54:EPS8^{FLAG} $^{MBP\text{-}His}$KCTD10	This Paper	N/A
$^{MBP\text{-}TEV}$KBTBD8	(Werner et al., 2018)	N/A
E1/UBA1	Laboratory of Michael Rape	N/A
UBE2D3/UBCH5C	Laboratory of Michael Rape	N/A
UBA3	Boston Biochem	Cat# E-313
UBE2M	Boston Biochem	Cat# E2-656

(*Continued on next page*)

Please cite this article in press as: Rodríguez-Pérez et al., Ubiquitin-dependent remodeling of the actin cytoskeleton drives cell fusion, Developmental Cell (2021), https://doi.org/10.1016/j.devcel.2021.01.016

Continued

REAGENT or RESOURCE	SOURCE	IDENTIFIER
NEDD8	Boston Biochem	Cat# UL-812
UBIQUITIN	Boston Biochem	Cat# U-100H
^{Methyl}Ubiquitin	Boston Biochem	Cat# U-501
Actin Protein (>99% Pure): Rabbit Skeletal Muscle	Cytoskeleton, Inc.	Cat# AKL99
Actin Protein (Pyrene Labeled): Rabbit Skeletal Muscle	Cytoskeleton, Inc.	Cat# AP05
ATP: 100mM Stock	Cytoskeleton, Inc.	Cat# BSA04
Alpha-Actinin Protein: Rabbit Skeletal Muscle	Cytoskeleton, Inc.	Cat# AT01
NAE Inhibitor MLN4924	Cayman Chemicals	Cat# 15217; CAS# 905579-51-3
Latrunculin A	Cayman Chemicals	Cat# 10010630; CAS# 76343-93-6
TEV protease	UC Berkeley QB3 MacroLab	N/A
Hoechst 33342	AnaSpec	Cat# 83218
cOmplete, EDTA-free protease inhibitor cocktail tablets from Roche	Sigma-Aldrich	Cat# 11873580001
Phenylmethanesulfonyl fluoride	Sigma-Aldrich	Cat# P7626
Polyethylenimine (PEI), Linear, MW 25000, Transfection Grade	Polysciences	Cat# 23966-1
Cycloheximide	Sigma-Aldrich	Cat# 01810; CAS# 66-81-9
Rhodamine Phalloidin	Thermo Fisher Scientific	Cat# R415
Alexa Fluor™ 488 Phalloidin	Thermo Fisher Scientific	Cat# A12379
Iodoacetamide	Thermo Fisher Scientific	Cat# A39271; CAS# 144-48-9
Protein G Agarose	Sigma-Aldrich	Cat# 11243233001
3xFlag peptide	Millipore	Cat# F4799
TCEP (Tris(2-carboxyethyl)phosphine hydrochloride))	Sigma-Aldrich	Cat# C4706; CAS# 51805-45-9
Carfilzomib	Selleck Chemical	Cat#PR-171; CAS# 868540-17-4
Lipofectamine RNAiMAX	Thermo Fisher Scientific	Cat# 13778150
Lenti-X concentrator	Takara	Cat# 631232
CellTracker™ Red CMTPX Dye	Thermo Fisher Scientific	Cat# C34552
CellTracker™ Green CMFDA Dye	Thermo Fisher Scientific	Cat# C7025
Ni-NTA	QIAGEN	Cat# 30210
Amylose Resin	New England Biolabs	Cat# E8021L
Critical Commercial Assays		
Pierce 660nm Protein Assay Reagent	Thermo Fisher Scientific	Cat# 22660
Ioninc Detergent Compatibility Reagent	Thermo Fisher Scientific	Cat# 22663
TnT quick coupled *in vitro* transcription/ translation system	Promega	Cat# L2080
SE Cell Line 4D-Nucleofector™ X Kit S	Lonza	Cat# V4XC-1032
Deposited Data		
Cul2 and Cul3 Adapter Myogenesis High-Content Screen	(Manford et al., 2020)	N/A
RNA-seq of C2C12 myoblasts depleted of KCTD10 at d0 or d2 of differentiation	GSE161681	N/A
Experimental Models: Cell Lines		
C2C12	ATCC	Cat# CRL-1772; RRID:CVCL_0188
HEK293T	ATCC	Cat#CRL-3216; RRID: CVCL_0063

(*Continued on next page*)

Please cite this article in press as: Rodríguez-Pérez et al., Ubiquitin-dependent remodeling of the actin cytoskeleton drives cell fusion, Developmental Cell (2021), https://doi.org/10.1016/j.devcel.2021.01.016

Continued

REAGENT or RESOURCE	SOURCE	IDENTIFIER
Mouse: Kctd10^{FLAG} C2C12 Cells	This Paper	N/A
Oligonucleotides		
KCTD10 endogenous tagging sgRNA: GTGCTCGGCCTGCTCACTGG	This Paper	N/A
ssODN for Endogenous Cell C-term KCTD10 3xFLAG tagging: GGAGCGGATCGAGCGCGTGA GGAGGATCCATATCAAGCGCC CAGATGACCGGGCCCACCTCCA CCAGGACTACAAAGACCATGAC GGTGATTATAAAGATCATGACA TCGATTACAAGGATGACGATG ACAAGTGAGCAGGCCGAGCAC CCTGCCTTCTGCCCTCCCTCTG CTCCTGCCCCGCCCCCTCAGA CCCTGTGC	This Paper	N/A
ON-TARGET plus siKCTD10 #1 mouse	Horizon Discovery	Cat# J-057526-05
ON-TARGET plus siEPS8 mouse	Horizon Discovery	Cat# J-045154-12
ON-TARGET plus siIRSp53 (Baiap2) mouse	Horizon Discovery	Cat# J-046696-11
ON-TARGET plus siIRTKS (BAIAP2L1) Mouse	Horizon Discovery	Cat# J-041646-12
ON-TARGET plus siACTN1 pooled mouse	Horizon Discovery	Cat# L-066191-00
ON-TARGET plus siACTN2 pooled mouse	Horizon Discovery	Cat# L-063823-01
ON-TARGET plus siKCTD13 pooled mouse	Horizon Discovery	Cat# L-055954-00
ON-TARGET plus siMYMX pooled mouse	Horizon Discovery	Cat# L-161743-00
Recombinant DNA		
pCS2+-^{HA}EPS8$^{(PH-L-PH)}$	This Paper	N/A
pCS2+-^{HA}EPS8$^{(PH1)}$	This Paper	N/A
pCS2+-^{HA}EPS8$^{(L)}$	This Paper	N/A
pCS2+-^{HA}EPS8$^{(PH2)}$	This Paper	N/A
pCS2+-^{HA}IRSp53	This Paper	N/A
pCS2+-^{HA}IRSp53$^{\Delta SH3}$	This Paper	N/A
pCS2+-^{HA}IRSp53$^{\Delta IMD}$	This Paper	N/A
pCS2+-^{HA}IRTKS	This Paper	N/A
pCS2+-^{HA}RHOB	This Paper	N/A
pCS2+-^{HA}STK3	This Paper	N/A
pCS2+-^{HA}PRKACA	This Paper	N/A
pCS2+-^{HA}PRKA2B	This Paper	N/A
pCS2+-^{HA}EPS8	This Paper	N/A
pLVX-TetOne-Puro-mCHERRY-KCTD10^{FLAG}	This Paper	N/A
pINDUCER20-KCTD10^{FLAG}	This Paper	N/A
pINDUCER20-KCTD10$^{\Delta CUL3}$	This Paper	N/A
pINDUCER20-EGFP-Ftractin	This Paper	N/A
pINDUCER20-EGFP-EPS8	This Paper	N/A
pINDUCER20-EPS8^{WT}	This Paper	N/A
pINDUCER20-EPS8^{RAFA}	This Paper	N/A
pINDUCER20-EPS8^{SATA}	This Paper	N/A
pINDUCER20-EGFP-[PH]$_2$-EPS8	This Paper	N/A
pINDUCER20-EPS8-OMP	This Paper	N/A
pINDUCER20-Ub-EPS8	This Paper	N/A
pINDUCER20-p18-IRSp53	This Paper	N/A

(*Continued on next page*)

Please cite this article in press as: Rodríguez-Pérez et al., Ubiquitin-dependent remodeling of the actin cytoskeleton drives cell fusion, Developmental Cell (2021), https://doi.org/10.1016/j.devcel.2021.01.016

Continued

REAGENT or RESOURCE	SOURCE	IDENTIFIER
pINDUCER20-IRSp53-OMP	This Paper	N/A
pMAL-$^{MBP/HIS}$KCTD10	This Paper	N/A
Split 'n coexpress CUL3-RBX1	(Zhuang et al., 2009)	RRID:Addgene_52293
pCOLA-Duet1-^{MBP}IRSp53/EPS8^{FLAG}	This Paper	N/A
Software and Algorithms		
Metamorph Advanced	Molecular Devices	RRID:SCR_002368
Columbus Image Data Storage and Analysis System	PerkinElmer	Cat# Columbus
Harmony High-Content Imaging and Analysis Software	PerkinElmer	Cat# HH17000010
Fiji	(Schindelin et al., 2012)	RRID:SCR_002285
Kallisto	(Bray et al., 2016)	RRID:SCR_016582
Sleuth	(Pimentel et al., 2017)	RRID:SCR_016883
CellTracker	(Piccinini et al., 2016)	N/A
MosaicSuite Particle Tracker plug-in	(Sbalzarini and Koumoutsakos, 2005)	N/A
CompPASS	(Huttlin et al., 2015)	N/A
Other		
HiLoad 16/600 Superdex 200pg	GE Healthcare	Cat#28-9893-35
HiLoad 16/600 Superose 6 pg	GE Healthcare	Cat# 29323952
4D-Nucleofector™ X Unit	Lonza	Cat# AAF-1002X

RESOURCE AVAILABILITY

Lead Contact

Further information and requests for reagents and resources should be directed to and will be fulfilled by the Lead Contact Michael Rape (mrape@berkeley.edu).

Materials Availability

All plasmids and cell lines generated in this work can be requested from the lead contact's lab. All antibodies, chemicals, and most cell lines used in this study are commercially available.

Data and Code Availability

Original gene expression data by RNA-seq from myoblasts or differentiating myocytes lacking KCTD10 (and corresponding controls) were uploaded to GSE161681

EXPERIMENTAL MODEL AND SUBJECT DETAILS

C2C12 myoblasts and HEK293Ts were grown in DMEM with 10% fetal bovine serum. For C2C12 differentiation, cells were grown to 70-90% confluence and had their media changed 2-3x in differentiation medium, DMEM 2% donor equine serum. For amino acid starvation, cells were washed 1x in PBS and put in amino acid free RPMI and 10% dialyzed FBS. 1x Amino acids were added to the cultures at indicated time points. For glucose and glutamine starvations, cells were rinsed in phosphate buffered saline and incubated with DMEM -Glucose or DMEM -Glutamine with 10% dialyzed fetal bovine serum.

METHODS DETAILS

Antibodies

The following antibodies were used in this study: α-Flag (Sigma, clone M2, F1804), α-CUL3 (A301-109A Bethyl), α-KCTD10 (HPA014273 SIGMA Prestige Antibodies), α-Myosin heavy chain, sarcomere (MHC) (MF20 Developmental Studies Hybridoma Bank (DHSB)), α-Myogenin (F5D DHSB), α-LAMP1 (1D4B DHSB), anti-β-ACTIN (MP Biomedicals, clone C4, 691001), α-HA-Tag (C29F4 Rabbit mAb #3724 Cell Signaling Technology (CST)), α-DYKDDDDK Tag (#2368 CST), α-IRSp53 (HPA023310 SIGMA Prestige Antibodies), α-TOMM20 (HPA011562 SIGMA Prestige Antibodies), α-IRTKS, (D1Z9C XP® Rabbit mAb #12721 CST), α- VINCULIN (E1E9V XP® Rabbit mAb # 13901 CST), α-EPS8 (610143 BD Transduction Labs), α-ESGP (MYMX) (AF4580 R&D Systems). α-Sarcomeric α-actinin clone EA-53 (A7811 Sigma Aldrich)

Please cite this article in press as: Rodríguez-Pérez et al., Ubiquitin-dependent remodeling of the actin cytoskeleton drives cell fusion, Developmental Cell (2021), https://doi.org/10.1016/j.devcel.2021.01.016

Individual siRNA sequences

The following ON-TARGETplus siRNA reagents were used (Horizon Discovery): KCTD10#1 (J-057526-05); EPS8 (J-045154-12); IRSp53 (J-046696-11); IRTKS (J-041646-12); ACTN1 (L-066191-00); ACTN2 (L-063823-01); KCTD13 (L-055954-00); TNFAIP1 (L-058905-00); MYMX (L-161743-00); non-targeting control #3 (D-001810-03)

Cloning

Kctd10, Eps8, Irsp53, Irtks, Rhob, Stk3, Prkaca, and Prka2b constructs were cloned from cDNA prepared from C2C12s. F-tractin was a generous gift from Matthew Welch. OMP and p18 sequences were a generous gift from Roberto Zoncu. All KCTD10, EPS8, and IRSp53 mutants, truncations, and fusion constructs were generated by overlap extension polymerase chain reaction, or site directed mutagenesis using quick change method. pINDUCER20 vectors were generated by first cloning constructs into pENTR1A entry vector, and then recombining into the destination vector pINDUCER20 (Meerbrey et al., 2011).

R_{MHC} index analysis

To obtain a quantitative metric to analyze cell roundness, indicative of aberrant cell fusion, we used a linear classifier based upon the Columbus image data storage and analysis system (PerkinElmer). We used siMYMX-differentiated myoblasts as a training set for unsupervised imaging analysis. This linear classifier and imaging analysis then formed the basis to analyze a C2C12 myogenesis screening data set that contained CUL2 and CUL3 adapters. Data are presented as mean ± SD. Statistical significance between groups was tested using an unpaired two-tailed Student's *t* test.

Fusion index analysis

As an orthogonal approach to quantify myogenesis phenotypes, including cell fusion, we used a fusion index. Fusion index was calculated as the number of nuclei inside myotubes (MHC^+ cells, containing $\geq$3 nuclei) over the total number of nuclei. Data are presented as mean ± SD. Statistical significance between groups was tested using an unpaired two-tailed Student's *t* test.

High content screening and myotube analysis

For high-content myogenesis screening, early passage C2C12 were seeded into 96 well plates at 400 to 500 cells/well using a Thermo Scientific Mulitdrop Combi system. The next day, cells were transfected with ~40nM final concentration of siRNAs using an Agilent Velocity 11 Bravo Automated Liquid Handling Platform. The next day, cells were differentiated by changing the media to differentiation media using the Bravo. Media was changed every day and on the fourth day, cells were fixed in 4% formaldehyde in phosphate buffered saline (PBS) for 20min. Cells were washed in PBS, permeabilized with 0.1% triton, and stained for immunofluorescence with antibodies in PBS with 10% fetal bovine serum. All incubations for immunofluorescence were done with very slow mixing in a circular motion (600 rpm) on an IKA 2/4 digital microtiter rotary plate shaker for 3h for primary antibody and 1h for secondary antibody and Hoechst (AnaSpec Inc.). Plates were imaged on an Opera Phenix (PerkinElmer) with a 10x objective capturing 25 images per well. Images were analyzed by an analysis sequence designed in the Perkin Elmer Harmony software using Columbus image data storage and analysis system (PerkinElmer).

Individual siRNA analysis was performed as described above, but with 12 well plates seeded with early passage C2C12 cells at 40,000-50,000 cells/well. The day after seeding, cells were transfected with 20-80nM final concentration of siRNAs depending on the number of co-depletions. Cells were fixed at day 4 of differentiation and prepared for immunofluorescence as described above. 49-100 images per condition were acquired on Perkin Elmer Opera Phenix automated microscope using a 20x objective and analyzed by an analysis sequence designed in the Perkin Elmer Harmony software or Columbus.

Cell culture

C2C12 myoblasts and HEK293Ts were grown in growth media (GM; DMEM with 10% fetal bovine serum). For C2C12 differentiation, cells were grown to 70-90% confluence and had their media changed 2-3x in differentiation medium (DM), DMEM + 2% donor equine serum. siRNA transfections were performed with Lipofectamine RNAiMAX (Thermofisher) according to manufacturer instructions.

Viral production

Lentiviral pLVX-TetOne-Puro-mCHERRY-KCTD10, pINDUCER20-KCTD10, pINDUCER20-KCTD10$^{\Delta CUL3}$, pINDUCER20-EGFP-FTractin, pINDUCER20-EGFP-EPS8, pINDUCER20-EPS8, pINDUCER20-EPS8^{RAFA}, pINDUCER20-EPS8^{SATA}, pINDUCER20-EGFP-$[PH]_2$-EPS8, pINDUCER20-EPS8-OMP, pINDUCER20-Ub-EPS8, pINDUCER20-p18-IRSp53, and pINDUCER20-IRSp53-OMP (pINDUCER from (Meerbrey et al., 2011)) were generated in 293T cells by co-transfection of pINDUCRER20 constructs with 3rd generation lentiviral packaging plasmids (Addgene) using PEI. Viral supernatants were collected and filtered through a 0.45μm PES filter and concentrated with LentiX concentrator following the manufactures protocol (Takara 631232). Precipitated virus was resuspended in GM, split into five (5) equal volume aliquots, and frozen.

Lentiviral spinfections

To generate C2C12 stable cell lines, one concentrated virus aliquot was added to 1.5 x 10^5 cells in 1.5 mL Eppendorf tube, supplemented with 10 μg/mL polybrene, to a 1 mL final volume with GM. Infection mixture was added to one well of a 12-well tissue culture plate, and spun at 1,000 x g for 90 min at 30 °C. Supernatant was removed and replaced with fresh GM + 10 mg/ml

Please cite this article in press as: Rodríguez-Pérez et al., Ubiquitin-dependent remodeling of the actin cytoskeleton drives cell fusion, Developmental Cell (2021), https://doi.org/10.1016/j.devcel.2021.01.016

insulin. Subsequently, cells were gently resuspended by pipetting up and down, and transferred to a 10 cm dish containing fresh GM + 10 mg/ml insulin. Selection was performed by adding 1 mg/mL of G418 (Thermofisher) to 10% FBS + DMEM, 48 h after spinfection. For construct expression, 1 μg/mL doxycycline was used.

For the generation of a stable cell line expressing both pINDUCER20-EGFP-EPS8 and pLVX-TetOne-Puro-mCHERRY-KCTD10, C2C12 cells were infected in series. A cell line expressing pINDUCER20-EGFP-EPS8 was generated using the procedure stated above with the following modifications: spinfections were performed in the presence of 20% FBS + DMEM, and 10 mg/ml of insulin. Cell were selected as stated above using G418. Upon selection, cells were re-infected using one concentrated virus aliquot of pLVX-TetOne-Puro-mCHERRY-KCTD10 in the presence of 20% FBS + DMEM and 10 mg/ml of insulin and following the spinfection protocol stated above. Selection was performed using 500 μg/mL of G418 and 1.5 μg/ml of puromycin in 10% FBS + DMEM. After 3 days, selection was changed to 500 μg/mL of G418 and 1 μg/mL of puromycin. After 3 days, selection was changed to 500 μg/mL of G418 and 0.75 μg/mL of puromycin.

Whole cell lysates

For Western blot time courses, C2C12 myoblasts were seeded in 12 well plates at 40-50k cells per well. Cells were transfected 24h later with indicated siRNAs at 20nM-40nM for each siRNA. 24h after transfection, cells were differentiated, harvested at indicated time points by washing in PBS, and lysed in 200μl 2x urea sample buffer, heated to 65°C for 10min, sonicated, and normalized to protein concentration and volume with Pierce 660nm Protein Assay Reagent (ThermoFisher 22660). Samples were analyzed by immunoblot with indicated antibodies.

In vitro ubiquitylation

For ubiquitylation reactions, CUL3-RBX1 and CUL3^{KCTD10} complexes were modified with NEDD8 prior to the ubiquitylation reaction, in 1x UBA buffer (50mM Tris-HCl pH 7.5, 50mM NaCl, 10mM $MgCl_2$), 20mM ATP, 6.3μM Nedd8, 1mM DTT, 5μM CUL3 complexes, 700nM UBA3, 400nM UBE2M in a 20μl reaction volume for 15min at 30°C. Ubiquitylation assays were carried out in 10μl reactions with 1μM CUL3 ligase, 100 μM ubiquitin, 1x UBA buffer (50mM Tris-HCl pH 7.5, 50mM NaCl, 10mM $MgCl_2$) 20mM ATP, 1mM DTT, 1μM UBCH5C, 1μM UBA1, 1 μM KCTD10, and 1 μM IRSp53:EPS8 complex. Reactions were carried out at 30°C for 1h, and subsequently quenched with 2x urea sample buffer.

In vitro binding

pCS2+-^{HA}EPS8, pCS2+-^{HA}EPS8$^{(PH-L-PH)}$, pCS2+-^{HA}EPS8$^{(PH1)}$, pCS2+-^{HA}EPS8$^{(L)}$, pCS2+-^{HA}EPS8$^{(PH2)}$, pCS2+-^{HA}IRSp53, pCS2+-^{HA}IRSp53$^{\Delta SH3}$, pCS2+-^{HA}IRSp53$^{\Delta IMD}$, pCS2+-^{HA}IRTKS, pCS2+-^{HA}RHOB, pCS2+-^{HA}STK3, pCS2+-^{HA}PRKACA, pCS2+-^{HA}PRKA2B was synthesized using the rabbit reticulocyte lysate TnT quick coupled *in vitro* transcription/translation system (Promega, L2080) as directed, using L-[^{35}S]-methionine. Translated construct reactions were diluted in binding buffer (25mM HEPES 7.5, 150mM NaCl, 0.2% NP40, 1 mM DTT) and added to amylose beads with bound ^{MBP}KCTD10 or MBP, or FLAG beads with bound ^{FLAG}KCTD10 or empty FLAG beads. Samples were rocked at room temperature for 1 h and washed in binding buffer. Samples were eluted in urea sample buffer and analyzed by autoradiography.

Immunofluorescence and confocal microscopy

C2C12s were seeded (5,000 cells/ml) on cover slips, treated with siControl, siKctd10, or co-depleted with siKctd10 and siEps8 for 48h, carfilzomib (10 nm) for 24h, or MLN-4924 (1 μM; 15217 Cayman Chemical) for 24h, or 100 ng/ml latrunculin A for 30min (10010630 Cayman Chemical). For localization experiments using pINDUCER20-KCTD10 (and associated mutants), pINDUCER20-p18-IRSp53, pINDUCER20-IRSp53-OMP, pINDUCER20-EPS8-OMP, pINDUCER20-Ub-EPS8, and pINDUCER20-EGFP-[PH]$_2$-EPS8, stable C2C12 cells were seeded (5,000 cells/ml for myoblasts, 50,000 cells/ml for myotubes) on cover slips and induced with doxycycline for 48 h. Cells were fixed in 4% formaldehyde in 1X PBS for 20 min at room temperature, permeabilized with 0.1% Triton X-100 in 1X PBS, blocked in 10% FBS in 1X PBS, stained with 1° antibodies for 3 h at room temperature, followed by staining with 2° antibodies and Hoechst stain or phalloidin. Samples were mounted onto coverslips and imaged using an Olympus IX81 microscope equipped with a Yokogawa CSU-1X confocal scanner unit (CSUX1 Borealis Square Upgrade Module), an ANDOR iXon3 camera (IXON DU-897-BV), and an Andor Technology Laser Combiner System 500 series equipped with four laser lines.

Myogenesis functional assays

pINDUCER20-KCTD10, pINDUCER20-KCTD10$^{\Delta CUL3}$, pINDUCER20-EPS8, pINDUCER20-EPS8^{RAFA}, pINDUCER20-EPS8^{SATA}, and pINDUCER20-Ub-EPS8 C2C12 stable cell lines were generated for myogenesis functional assays. All cell lines were seeded on 12-well plates (50,000 cells/ml), and expression was induced with doxycycline during seeding when necessary. siRNA depletions were done 24 h after seeding, with siControl, siKctd10, siEps8, or siKctd10 + siEps8. For siKctd10 rescue assays, pINDUCER20-KCTD10 and pINDUCER20-KCTD10$^{\Delta CUL3}$ cell lines were treated with doxycycline either during seeding or 48h after differentiation. Cells were fixed in-well in 4% formaldehyde in 1X PBS for 20min at room temperature, permeabilized with 0.1% Triton X-100 in 1X PBS, blocked in 10% FBS in 1X PBS, stained with 1° antibodies for 3h at room temperature, followed by staining with 2° antibodies and Hoechst stain or phalloidin. Samples imaged using a Perkin Elmer Opera Phenix, and data was analyzed using the Columbus image analysis software.

Please cite this article in press as: Rodríguez-Pérez et al., Ubiquitin-dependent remodeling of the actin cytoskeleton drives cell fusion, Developmental Cell (2021), https://doi.org/10.1016/j.devcel.2021.01.016

Live cell imaging

Stable C2C12 cells expressing pINDUCER20-EGFP-FTractin, pLVX-TetOne-Puro-mCHERRY-KCTD10 or pINDUCER20-EGFP-EPS8 were seeded (5,000 cells/ml for pINDUCER20-EGFP-FTractin, and 50,000 cells/ml for pINDUCER20-EGFP-EPS8) on 4-well live-cell imaging chambers (Nunc™ Lab-Tek™ II Thermo). Double infected cell lines expressing pLVX-TetOne-Puro-mCHERRY-Kctd10 or pINDUCER20-EGFP-EPS8 were seeded at 5,000 cells/ml on 4-well live-cell imaging chambers (Nunc™ Lab-Tek™ II Thermo). For all cell lines, expression was induced with doxycycline (1 μg/ml) the same day cells were seeded. pINDUCER20-EGFP-FTractin stable cells were treated with siControl or siKctd10 for 48 h before imaging. pINDUCER20-EGFP-EPS8 stable cells were differentiated for 2 days in DM prior to image acquisition.

For time lapse imaging acquisition, chambers were placed in a temperature and humidity controlled chamber with 5% CO_2. Laser power was kept at 25% for all imaging using the aforementioned spinning disc confocal imaging system.

Cell mixing assays

Myogenesis asymmetry assays were performed by mixing two C2C12 populations differentiated at different times. A founder myotube (FM) population and a fusion competent myoblast (FCM) population were established and mixed. The FCM population was generated by seeding myoblasts at a low concentration (20,000 cells/mL), FM population was generated by seeding at a high density (35,000 cells/mL). FM population was switched to DM media 48 h after seeding, while the FCM population was kept in GM media. Both population were treated with siControl or siKctd10 2 days after the FM population was switched to DM. 20 h after siRNA treatments, FM and FCM cell populations were treated for 45 min with 10 μM of CellTracker™ CMPTX or CMFDA dyes following manufacturer recommendations. Cell populations were allowed to recover for 4 h to allow for any residual dye to be incorporated prior to population mixing. Populations were then mixed by trypsinizing the FCM population and adding to the corresponding FM populations. Cells were kept in DM media for 2 additional days prior to fixing in 4% formaldehyde. Cells were stained and imaged as described above.

Cell and particle tracking

Cell tracking of pINDUCER20-EGFP-FTractin was done using the CellTracker software (Piccinini et al., 2016). Particle tracking of pLVX-TetOne-Puro-mCHERRY-KCTD10 was performed using the FIJI plug image analysis software and the MosaicSuite Particle Tracker plug-in (Sbalzarini and Koumoutsakos, 2005).

Protein purifications

Mouse $^{MBP/HIS}$KCTD10 (pMAL, New England Biolabs) and the ^{MBP}IRSp53/EPS8^{FLAG} complex (pCOLAduet-1) were purified from *E.coli* LOBSTR cells grown to OD_{600} 0.5 and induced with 500 μM IPTG overnight at 16°C. Constructs were either purified separate or together. Cells were lysed in lysis buffer (50mM HEPES 7.5, 400 mM NaCl 1.5mM PMSF, 15mM β-mercaptoethanol, 10 mg/ml lysozyme, 30mM imidazole) for 45 min at 4 °C. Cells were sonicated and spun at 30,000xg for 1h. Supernatant was added to Ni-NTA slurry and bound for 1h at 4°C. Beads were washed in wash buffer (50mM HEPES 7.5, 400mM NaCl, 5mM β-mercaptoethanol, 20mM imidazole) three times for 15min with rocking. Beads were eluted with 50mM HEPES 7.5, 400mM NaCl, 5mM β-mercaptoethanol, 250mM imidazole. Elutions were dialyzed overnight and run on a HiLoad 16/600 Superdex 200pg or HiLoad 16/600 Superose 6 prep grade, concentrated, aliquoted, and flash frozen. For CUL3-RBX1 purification, split $^{GST\text{-}TEV}$-CUL3 and untagged RBX1 were purified as previously described (Werner et al., 2018). Briefly: *E.coli* LOBSTR cells grown to OD_{600} 0.5 and induced with 500 μM IPTG overnight at 16°C. Cells were lysed in lysis buffer (50mM HEPES 7.5, 200 mM NaCl 1.5mM PMSF, 15mM β-mercaptoethanol, 10 mg/ml lysozyme) for 45min at 4 °C. Cells were sonicated and spun at 30,000xg for 1h. Supernatant was added to glutathione beads for 2h at 4°C. Beads were washed in wash buffer (50mM HEPES 7.5, 400mM NaCl, 5mM β-mercaptoethanol) three times for 15min, with rocking. TEV protease was added to beads (at 1ug:100ug TEV to protein ratio), and rocked overnight at 4 °C. Supernatant was collected and run on a HiLoad 16/600 Superdex 200pg, concentrated, aliquoted, and flash frozen.

Endogenously tagged ^{FLAG}KCTD10 for IVT binding experiments was purified from C2C12 cells using affinity-purification as performed for large-scale immunoprecipitations, except ^{FLAG}KCTD10 was not eluted from beads and directly used for binding experiments.

E1/UBA1, UBE2D3, and MBP-KBTBD8 were purified previously described (Jin et al., 2012; Mena et al., 2018; Wickliffe et al., 2011). The neddylation machinery (human UBA3 (E1), UBE2M (E2), NEDD8) and ubiquitin were purchased from Boston Biochem.

Actin polymerization and bundling assays

For actin polymerization assays, pyrene muscle actin (AP05 Cytoskeleton) was prepared according to manufacturer's instructions. Briefly, actin was diluted to 0.45 mg/ml using general actin buffer (5 mM Tris-HCl 8.0, 0.2 mM $CaCl_2$, 0.2 mM ATP, 1 mM DTT) and depolymerized on ice for 30min. Residual nuclei were removed by spinning at 21,000 x *g* at 4 °C for 30min. Actin was then mixed with 0.5 μM or 1 μM KCTD10:EPS8:IRSp53, or 1 μM IRSp53, or 1 μM KCTD10, or 1 μM EPS8:IRSp53, for 15 min. Polymerization was induced by adding 10x acting polymerization buffer (1x final; 500 mM KCl, 20 mM $MgCl_2$, 10 mM ATP). Actin polymerization was tracked by using a BioTek Synergy H4 plate reader, taking readings every 30 s for 1h, with an excitation wavelength of 360 nm and emission of 405 nm.

Actin bundling experiments were performed using α-actinin (AP05 Cytoskeleton) according to manufacturer's instructions. Briefly, F-actin was prepared by polymerizing 1 mg/mL muscle actin (AKL99 Cytoskeleton) in actin polymerization buffer (1X final) for 1h at

Please cite this article in press as: Rodríguez-Pérez et al., Ubiquitin-dependent remodeling of the actin cytoskeleton drives cell fusion, Developmental Cell (2021), https://doi.org/10.1016/j.devcel.2021.01.016

room temperature. To bundle actin, 10 μM F-actin is mixed with 2 μM α-actinin, or 2 μM KCTD10:EPS8:IRSp53 complex, or EPS8-IRSp53 complex, or ubiquitylated EPS8-IRSp53 complex, or 2 μM BSA for 30min. For co-bundling assays, F-actin was co-incubated with 2 μM α-actinin along with 2 μM BSA or KCTD10:EPS8:IRSp53 complex, or KCTD10:EPS8:IRSp53 complex was added after bundling with α-actinin.

For spin-down bundling assays, samples were spun at 100,000 x *g* for 1h. The supernatant was carefully removed and resuspended in 2x urea sample buffer. The remaining pellet was resuspended in 1x urea sample buffer (final volume should be the same as supernatant + urea sample buffer volume). Samples were then analyzed by SDS-PAGE and stained with coomassie. For imaging-based bundling assays, reactions were treated with rhodamine-phalloidin (1:500 dilution) for 15min. Reactions were then added to coverslips functionalized with poly-D-lysine, and subsequently mounted onto coverslips. Coverslips were imaged using the aforementioned spinning disc confocal imaging system.

Immunoprecipitation and mass spectrometry

For endogenous ^{FLAG}KCTD10 affinity-purifications, cells were pre-treated with 1 μM MLN-4924 for 16 h. For all stable cell line experiments, cells were treated with doxycycline (1 μg/ml) for 48 h to induce expression of constructs.

Large scale immunoprecipitations were performed after harvesting cells in cold PBS (150 plates of C2C12 cells for endogenously tagged ^{FLAG}KCTD10; 75 plates for stable C2C12 cell lines) and centrifuging them at 300g for 10min. Cell pellets were resuspended in 5x the volume of pellet weight (ml/g) of lysis buffer (40mM HEPES 7.5, 150mM NaCl, 0.2% NP40, with Roche cOmplete Protease Inhibitor Cocktail). Lysates were gently rocked for 1h at 4°C and cleared by centrifugation at 500g, 5 min and 21000g, 30min. Supernatants were pre-cleared by incubating them with protein G agarose beads for 30 min. Subsequently, supernatants were added to 90μl of α-FLAG® M2 Affinity Agarose Gel slurry (Sigma A2220) and rotated for 1-2h at 4°C. Beads were washed extensively in lysis buffer and eluted 2x with 250μl of 3xFLAG peptide (F4799, Millipore). Elutions were pooled and precipitated overnight on ice with 20% trichloroacetic acid. The precipitated pellets were washed in acetone, dried, and solubilized in 8M urea, 100mM TRIS, pH 8.5. The samples were reduced with TCEP, alkylated with iodoacetamide, and digested overnight with trypsin (V5111, Promega). Trypsinized samples were analyzed by Multidimensional Protein Identification Technology (MudPIT) at the Vincent J. Coates Proteomics/Mass Spectrometry Laboratory at UC Berkeley. Unique proteins were identified by comparing each IP to a dataset of 40-150 similar (unique databases for C2C12) αFLAG IP/mass spectrometry samples using CompPASS analysis by using the R specific package ComPASS (Huttlin et al., 2015). All total spectral counts were normalized to 1000 TSC of bait.

For endogenous immunoprecipitation of EPS8, C2C12s were grown to 80% confluence and treated with 1 μM MLN-4924 for 16 h. Antibodies were conjugated to protein G agarose beads for one hour at 4°C prior to immunoprecipitation. Cells were harvested and lysed as described above. 50% of the supernatant was incubated with 2.5μg of α-EPS8 antibody (610143 BD Transduction Labs) or normal mouse IgG pre-conjugated to protein G agarose beads for 1.5h at 4°C. After incubation, samples were washed with lysis buffer three times. Beads were resuspended in 1x urea sample buffer in preparation for western blot analysis.

Genome editing

Endogenous ^{3xFLAG}Kctd10 C2C12 cell lines were generated using the ribonucleoprotein (RNP) method (DeWitt et al., 2017) using a guide targeting the exon 7 of Kctd10, at the junction between the 3' UTR and the coding region of exon 7 (5'-GTGCT CGGCCTGCTCACTGG-3') and a 200 bp ssODN repair template containing the 3xFLAG (5'-GGAGCGGATCGAGCGCGTGAGGAG GATCCATATCAAGCGCCCAGATGACCGGGCCCACCTCCACCAGGACTACAAAGACCATGACGGTGATTATAAAGATCATGACATC GATTACAAGGATGACGATGACAAGTGAGCAGGCCGAGCACCCTGCCTTCTGCCCTCCCTCTGCTCCTGCCCCGCCCCCTCAGAC CCTGTGC-3'). Guide RNAs were synthesized with NEB HiScribe T7 High Yield RNA Synthesis Kit, DNAse treated with turboDNAse (Ambion/Thermo), and purified with the Invitrogen MEGASCRIPT clean-up kit. RNPs were assembled with Cas9 purified by the UC Berkeley QB3 MacroLab in a 10 μl reaction of 100 pmol of Cas9, 120 pmol sgRNA, and 100 pmol ssODN in Cas9 buffer (20 mM HEPES 7.5, 150 mM KCl, 10% glycerol, 1 mM TCEP). Reactions were gently mixed for 30s and incubated for 10min at room temperature. RNP complexes and 100k C2C12s cells resuspended in 20 μl buffer SE (Lonza) were added to a nucleofection strip and the mixture pulsed with program CD-137 (Lonza 4D-Nucleofector). Cells were plated into 6-well dishes. After confirmation of bulk editing by PCR, cells were diluted to 5cells/ml and 100μl of cell suspension was plated per well plated into 96 well plates containing 200μl total media, 20% FBS DMEM + Pen/Strep. Colonies were expanded and screened for 3xFLAG tagging by PCR and Western blot, and confirmed by DNA sequencing.

NGS Library Prep and RNA-seq

Total RNA was extracted from sub-confluent C2C12s and C2C12s differentiated for 2 days, treated with siKctd10, or siControl siRNAs (in triplicate) using a NucleoSpin Plus RNA extraction kit (Machery-Nagel). NGS libraries were made using a TruSeq Stranded Total RNA kit (Illumina), with an average size of 250 bp. Libraries were prepared by the UC Berkeley Functional Genomics Laboratory. Paired-end RNA-sequencing was done using a HiSeq400 (Illumina).

RNA-seq Alignment and Expression Analysis

We used the Kallisto-Sleuth pipeline to perform differential gene expression analysis between samples (Pimentel et al., 2017). Briefly, paired-end RNA-seq reads were aligned using Kallisto, using the mm10 *Mus musculus* reference transcriptome and 200 bootstrap

steps. For differential expression analysis, the R Sleuth package was used. To obtain $\log_2$ fold changes, we had to implement the following transformation function during the initial sleuth object (so) preparation step:

so <- sleuth_prep(s2c, ~ condition / bio_samp, extra_bootstrap_summary = TRUE, target_mapping = t2g, transformation_function = function(x) $\log_2$(x + 0.5))

To identify significant differentially expressed genes, the following conditions were compared: siControl v siKCTD10. From each comparison, significant differentially expressed genes with a qval $\leq$ 0.075 were kept.

Transmission and scanning electron microscopy

For transmission electron microscopy, C2C12 cells were grown on Aclar discs, treated with siControl or siKctd10, and differentiated for two days in DM media. Stable C2C12s infected with pINDUCER20-OMP-IRSp53 (treated with 1 μg/ml dox) were grown to 60% confluence before fixation. Cells were fixed in 2% glutaraldehyde: 0.1 M sodium cacodylate (pH 7.2) for 20 min, followed by 3 washes with 0.1 M sodium cacodylate buffer. For stable cell lines, cells were gently harvested and collected in 1.5 mL Eppendorf tubes, followed by imbedding in agarose plugs (this was not done for cells grown on Aclar discs). After solidifying, agar plugs containing the specimens were carefully cut into ~2.5 mm^3 slices. Discs or agar plugs were stained in 1% osmium tetroxide in 0.1 M sodium cacodylate for 1 hr, followed by 1.38% potassium ferricyanide for 1 hr. Stained samples were step-dehydrated in acetone (35%, 50%, 70%, 80%, 95%, 100%, 100%) for 10 min at each step. Dehydrated samples were then step-infiltrated with acetone:Epon resin (2:1, 1:1, 1:2 for 1 hr each). After final acetone:resin infiltration, samples were embedded in pure Epon resin at room temperature, overnight, followed by curing at 65 °C for two days. Cured samples were then sliced using a Leica UC 6 microtome, taking 70 nm sections. Sliced sections were picked up on 100 mesh formvar-coated copper grids, then stained with 2% aqueous uranyl acetate for 5 min, followed by 2% lead citrate for 2 min. Grids were examined under a Tecnai 12 TEM at 120 kV.

For scanning electron microscopy, C2C12s were seeded onto carbon conductive tabs and treated with siControl or siKctd10 for 48h, until they reached 60% confluency. Cells were fixed and stained as described above in 2% glutaraldehyde: 0.1 M sodium cacodylate (pH 7.2) and 1% osmium tetroxide in 0.1 M sodium cacodylate. After osmium staining and rinsing, samples were step dehydrated in ethanol (35%, 50%, 70%, 80%, 95%, 100%, 100%) for 10 min at each step. Dehydrated samples were critical point dried for 60 min, and subsequently sputter coated with a thickness of 2 nm. Samples were imaged using HITACHI S-5000 at 1 kV.

QUANTIFICATION AND STATISTICAL ANALYSIS

The quantifications presented in this study are shown as the mean ± standard deviation (SD). Statistical significance for mass spectrometry experiments was determined by a Wald test. All myogenesis quantifications represent at least 3 biological replicates, where significance was determined by a 2-tailed t-test (*p<0.05, **p<0.01, ***p<0.001). Figure 1A is a 2 biological replicate screen done in duplicate. EPS8/KCTD10 live-cell membrane exchange assays were quantified by doing a line-scan and measuring the intensities of each channel. Each channel was normalized to its cytoplasmic intensities. Quantifications are the mean ± SD of two biological replicates. Actin polymerization assays are depicted as the mean ± SD of 3 wells per condition, performed in duplicate (two biological replicates of three technical replicates). Cell motility assays were measured as the total distance displaced as measured by the CellTracker algorithm. For each condition, 3 biological replicates were performed, where 5 fields containing at least 10 cells were measured. Significance testing was done by performing a one-way ANOVA (*p<0.01, **p<0.001, ***p<0.0001, ****p<0.00001). For cell heights assays, measurements were done in Fiji by measuring from the base of the cell to the apex of the cell. 3 biological replicates were performed per condition, with at least 15 specimens per replicate. Significance testing was done by performing a 2-tailed t-test (*p<0.05, **p<0.01, ***p<0.001, ****p<0.0001).